PREDICTION OF THE PERFORMANCE OF AN ION THRUSTER USING BUCKMINSTERFULLERENE AS PROPELLANT

by

ESTEBAN RAUL TORRES

B.S., Aeronautics and Astronautics
Massachusetts Institute of Technology, 1991

Submitted to the Department of Aeronautics and Astronautics
in Partial Fulfillment of the Requirements for the Degree of

MASTER OF SCIENCE
in Aeronautics and Astronautics
at the

Massachusetts Institute of Technology

February 1993

Copyright Esteban R. Torres 1993
All rights reserved

The author hereby grants MIT permission to reproduce and to distribute publicly copies of this thesis document in whole or in part.

Signature of Author________________________________
Department of Aeronautics and Astronautics
November 9, 1992

Certified by________________________________ 11/16/92
Manuel Martinez-Sanchez
Associate Professor of Aeronautics and Astronautics
Thesis Supervisor

Accepted by________________________________
Professor Harold Y. Wachman
Chairman, Department Graduate Committee

MASSACHUSETTS INSTITUTE
OF TECHNOLOGY

FEB 17 1993

LIBRARIES

ARCHIVES

PREDICTION OF THE PERFORMANCE OF AN ION THRUSTER USING BUCKMINSTERFULLERENE AS PROPELLANT

by

ESTEBAN RAUL TORRES

Submitted to the Department of Aeronautics and Astronautics
on November 9, 1992 in partial fulfillment of the
requirements for the Degree of Master of Science in
Aeronautics and Astronautics

ABSTRACT

A theoretical investigation was carried out to predict the performance of an electron bombardment, ring-cusp ion thruster using buckminsterfullerene (C_{60}) as the propellant gas. The cross-sections for ionization of C_{60} molecules by collisions with electrons were obtained from the scientific literature, while the excitation cross-sections were calculated using a classical theory developed by Gryzinski. The thruster chosen was the Hughes 13 cm laboratory-model thruster. Brophy's model was then used to calculate the beam ion production cost as a function of the propellant utilization efficiency.

The results show that the baseline plasma ion energy cost of C_{60} is approximately the same as that of xenon. However, the primary electron utilization factor for the Hughes 13 cm lab-model thruster using C_{60} is 273 A^{-1}, which is 22 times that of xenon. Furthermore, the beam ion production cost at a 90 % propellant utilization using C_{60} was calculated to be 177 eV/beam ion, which is smaller than the 400 eV/beam ion obtained when using xenon. Brophy's model also shows that an optimum discharge voltage exists using C_{60} equal to 22 V. Because of this superior performance, the theory predicts that the thrust to power ratio of a C_{60} ion thruster is 1.5 times that of a Russian SPT-100 thruster producing the same thrust and I_{sp}.

Even though Brophy's model was applied to the Hughes 13 cm lab-model thruster, the results can be easily used for any other thruster.

Thesis Supervisor: Dr. Manuel Martinez-Sanchez

Title: Associate Professor of Aeronautics and Astronautics

Acknowledgements

After completing this work, I looked back to when I started and realized that it could not have been accomplished without the support, friendship, and help of friends. I must thank the Hughes Research Laboratories (HRL), especially Dr. Julius Hyman, for funding this research by a Hughes Masters' Fellowship sponsored through his department. In times of economic trouble when companies are shutting down or laying off people and money is tight, Hughes stood strong for me

I must also thank Dr. John R. Beattie (Bob) for allowing me to work in the Plasma Sources Group at HRL and opening my eyes to the wonders of ion propulsion. Furthermore, I am in great debt to Dr. Jesse Matossian and Dr. John D. Williams. Their insights into ion propulsion helped me to plan out this work. They took time from their projects to explain and teach me things, when I was breaking my brains to figure things, and I found sanctuary in their help. I found their devotion to their work inspiring and something that I want to imitate.

I also wish to say thank you to Manuel Martinez-Sanchez, whom I not only considered a Professor but also a friend, for supervising my work and putting up with all my groans and problems with graduate life here at MIT.

Finally, I must say thanks to my parents, Esteban and Maria, whose sacrifices allowed me to study at MIT, my elder sister to study medical school, and baby sister to attend private school, seven years after we had come to this country. Their warmth and support cannot be matched.

Table of Contents

List of Figures

List of Tables

Nomenclature

A_A	Anode wall surface area.
A_g	Area of the grids.
C_o	Primary electron utilization factor.
E	Energy of incoming electron.
e	Electron charge, 1.6×10^{-19} C.
ε_B	Beam ion production cost.
ε_p	Plasma ion energy cost.
ε_p^*	Baseline plasma ion energy cost.
ε_M	Thermal energy of Maxwellian electrons.
f_A	Fraction of ions collected by anode potential surfaces.
f_B	Fraction of ions extracted to form the beam.
f_C	Fraction of ions collected by cathode potential surfaces.
f_{ACC}	Fraction of ions that strike the accelerator grid.
ϕ_i	Transperancy of the ion optics system to ions.
ϕ_o	Transperancy of the ion optics system to neutrals.
Γ_i	Flux of ions across grids.
Γ_n	Flux of neutral across grids.
HOMO	Highest Occupied Molecular Orbital.
h	Planck's constant, 6.6×10^{-34} J·sec.
I_{sp}	Specific impulse.
J_A	Ion current collected by the anode potential surfaces.
J_B	Beam current.
J_C	Ion current collected by the cathode potential surfaces.
J_D	Discharge current.
J_E	Hollow cathode emission current.
J_o	Rate of flow of neutrals across the grids.
$J_{+,p}$	Rate of ion production by primary electrons.
$J_{exc,p}$	Rate of excitation of neutrals by primary electrons.
l_e	Primary electron containment length.
LUMO	Lowest Unoccupied Molecular Orbital.
k	Boltzmann's constant, 1.38×10^{-23} J/K
$\dot{m}$	Propellant mass flow rate.

η_u	Propellant utilization efficiency.
n_o	Density of neutrals inside the discharge chamber.
n_M	Density of Maxwellian electrons inside the chamber.
n_P	Density of primary electrons inside the chamber.
n_i	Density of ions in the beam.
σ_{exc}	Total excitation cross-section by collision with electrons.
$\sigma_{t,p}$	Total inelastic cross-section at the energy of primary electrons.
$\sigma_{j,p}$	Excitation cross-section of the jth excited state at the primary electron energy.
$<\sigma_+ v_e>$	Ionization rate coefficient by electrons.
$<\sigma_+ v_e>_M$	Ionization rate coefficient by Maxwellian electrons.
$<\sigma_j v_e>$	Excitation rate coefficient by electrons.
$<\sigma_j v_e>_M$	Excitation rate coefficient by Maxwellian electrons.
U_+	Ionization potential (also referred to as the ionization threshold energy).
U_j	Energy require to excite the jth excited state.
U_{ex}	Lumped excitation energy.
U_p^i	Ionization potential of energy level p
$U_{p,q}$	Energy difference between level p and q.
U_l	Excitation potential (also referred to as the excitation threshold energy).
ΔV_A	Potential difference between plasma potential and anode potential.
V_B	Beam voltage.
V_C	Potential of hollow cathode discharge region.
V_D	Discharge voltage.
V_S	Potential of screen grid.
V_A	Potential of accelerator grid.
v_b	Bohm velocity.
v_B	Velocity of beam ions.
v_e	Velocity of electrons.
v_p	Velocity of primary electrons.
V	Ion production volume.
ζ_e	Partition function of electron.
$\zeta_{C_{60}}$	Partition function of C_{60} molecules.
$\zeta_{C_{60}^-}$	Partition function of negative C_{60} ions.
$[C_{60}]$	Density of C_{60} molecules in the chamber.
$[C_{60}^-]$	Density of negative C_{60} ions in the chamber.

Chapter 1. Introduction

The 1960's and 1970's was a golden age for space exploration and research marked by Apollo landings on the moon and the Mariner landings on the Martian surface. The 1980's saw space program of a lower profile, but still a steady pace toward exploration was maintained through the development of the Space Shuttle. For the 1990's and beyond missions are being planned today that would benefit from the flight development of new propulsion systems. Missions where the trip time is long or where trip time is not an issue, such as in the case of interplanetary exploration or the orbit raising of large structures, are well-suited for electric propulsion systems. Likewise, missions where the amount of propellant that must be carried on board is extremely large, such as in the long term stationkeeping of a telecommunications satellite, could also benefit from electric propulsion. Ion thrusters, with a wide range of high potential specific impulses from 1000 to 6000 sec, offer a definite advantage over both conventional chemical thrusters and other types of electric propulsion schemes [1].

Section 1.1. Electric Propulsion

Specific impulse I_{sp} is a useful parameter for comparing the performance of different propulsion systems. It is defined as the ratio of the thrust of a rocket to the weight flow of the propellant. The advantage of high specific impulse can be illustrated through the rocket equation,

$$\frac{M_f}{M_i} = \exp\left(\frac{-\Delta v}{g_o I_{sp}}\right) ,$$

where Δv is the velocity change for a specific maneuver, g_o is the sea-level gravitational constant, M_f is the final mass of the spacecraft, and M_i is the initial mass. For a mission with a given Δv, the higher the specific impulse is the higher is the final mass of the spacecraft relative to its initial mass. By definition, the specific impulse is related to the exhaust velocity v_e of a thruster through the expression $I_{sp} = g_o v_e$.

Conventional thrusters, such as the Space Shuttle Main Engines (SSME) or the RL10 upper stage rocket motor, are handicapped by their exclusive reliance on combustion to accelerate the propellant gas. Fuel is mixed with its oxidizer in the chamber creating a chemical reaction. The energy released during the reaction increases the enthalpy of the newly formed propellant gas. As this gas expands through the nozzle, the enthalpy is converted to kinetic energy and finally to thrust as the gas exits the nozzle. Therefore, the exit velocity depends directly on the energy content of the fuel/oxidizer mixture. The search for energy-rich fuels has led to the use of hydrogen/oxygen, which in the case of the SSME the attained specific impulse is about 455 sec. However, it seems very unlikely that a specific impulse greater than 600 sec can be achieved using conventional chemical propulsion concepts. New approaches are needed.

Electric propulsion is defined as "the acceleration of gases for propulsion by electrical heating and/or by electric and magnetic body forces" [2]. The high exhaust velocities achievable by propulsive schemes utilizing electric propulsion offer significant savings in the mass of a spacecraft. In other words, for the same mission an electric thruster utilizes less propellant mass than a conventional thruster. This decrease in propellant could be translated into a higher payload mass or a lower initial mass of the spacecraft and thus reducing costs.

Currently there are two main drawbacks inherent in any electric propulsion scheme. One is the limited source of power available in space. In order to provide the kilowatts of power required to run a thruster, space power supplies tend to be large, heavy, and inefficient which erode the mass advantages gained through the high exhaust velocity. This drawback will be lessened through technological advances in power supplies and incorporating the power supplies into the overall mission. Likewise, thrusters using electric propulsion are plagued by extremely low mass flow rates of the propellant during efficient operation. Hence, electric propulsion thrusters are also characterized by low thrust when compared to conventional ones.

Three different categories of electric propulsion devices can adequately describe the wide range of electric propulsion thrusters that have so far been developed. These are electrothermal, electromagnetic, and electrostatic.

In an electrothermal thruster, electrical energy is used to heat the propellant gas to a very high temperature, and then the gas expands through the nozzle in order to create thrust. Resistojets and arcjets are two different types of electrothermal rockets that have been developed. The difference between them is the means of converting the electrical power to heat the propellant gas. Resistojets have a specific impulse comparable to that of conventional thrusters and are well-suited for such applications as attitude control, stationkeeping, and drag makeup [3]. They have been baseline to meet some of propulsive needs of the Space Station Freedom. On the other hand, arcjets offer specific impulses on the range between 460 and 1100 secs depending on the type of arcjet and the input power. Although they have never flown in space, a 1.8-kW hydrazine arcjet is scheduled to provide the stationkeeping needs of the GE Astro Space Series 7000 satellite. The first of these satellites is scheduled to fly in 1993 as an AT&T's Telstar 4 communications satellite. Moreover, arcjets are scheduled to be the primary propulsion scheme in the Air Force Electric Insertion Transfer Experiment (ELITE) to be launched in 1995. This program would demonstrate the technologies needed for an electric orbit transfer vehicle.

In an electromagnetic thruster, an ionized gas is accelerated through the interaction between the electric current conducted through the gas-discharge and a magnetic field. These devices require very high power on the order of 100 kW at a minimum (for good efficiencies, power levels of megawatts), and are at a very early stage of development. No electromagnetic thruster has ever being flight qualified or flown in space, except for a Japanese device which will fly in their ATS satellite. They produce thrust on the order of tens of newtons and are envisioned for far-term applications, including planetary exploration, orbit raising, and maneuvering.

Electrostatic thrusters use electric power to accelerate charged particles through perforated grids in order to produce thruster. Different schemes to implement electrostatic propulsion have been developed in the past. Colloid thrusters used charged, relatively massive, multi-atom particles called colloids as the propellant. Ion thrusters, on the other hand, rely on charged single atoms. Moreover, three different ways to ionize the propellant gas have been developed, i.e., contact ionization, radio-frequency ionization, and electron bombardment. Contact ionization results from the interaction of a single propellant atom with a suitable hot surface [4]. These types of thrusters were heavily studied in the 1960's and 1970's, but they have faded away since they could not match the capabilities offered by electron bombardment ion thrusters. Furthermore, radio-frequency ionization gives performance comparable to conventional bombardment thrusters and have been mainly pursued in Germany through the RIT series thrusters.

Section 1.2. Electron Bombardment Ion Thruster

The electron bombardment ion thruster is one of the best developed types of electric propulsion devices. Since first conceived in the 1950's, it has evolved through refinements. Figure 1.1 shows a state of the art xenon ion propulsion system. A typical ion propulsion system can be divided into four separate parts depending on the function, i.e. the discharge chamber, the ion optics system, the neutralizer, and the required power supplies. The discharge chamber is responsible for creating the ions, while the ion optics system extracts and accelerates the ions away from the spacecraft in order to produce thrust. The neutralizer in turns provides a stream of electrons that prevents the spacecraft from charging. Finally, the power supplies provide the power required to operate all parts of the ion propulsion system.

The discharge chamber is a coffee can-shaped cylinder, which houses all structures required to produce the ions. A common discharge chamber is sketched in Figure 2.1 in Chapter 2. Inside it there is a hollow cathode, which emits high energy electrons that collide with the propellant atoms in order to ionize them. Other schemes of supplying the electrons, such as refractory metals and oxide cathodes, were developed in the past. However, hollow cathodes have replaced these schemes because their long lifetimes (10,000 hours for flight qualified ones) are comparable to the missions proposed for ion propulsion. Furthermore, since the density of neutral atoms inside the discharge chamber is on the order of 10^{18} cm^{-3}, the mean free path for ionization of neutral atoms by electrons is on the order of meters; yet the length of the discharge chamber is usually less than 30 cm. In order to constrain the electrons within the chamber and restrain them from being lost to the anode, a magnetic field is employed as shown in Figure 3.2 in Chapter 3.

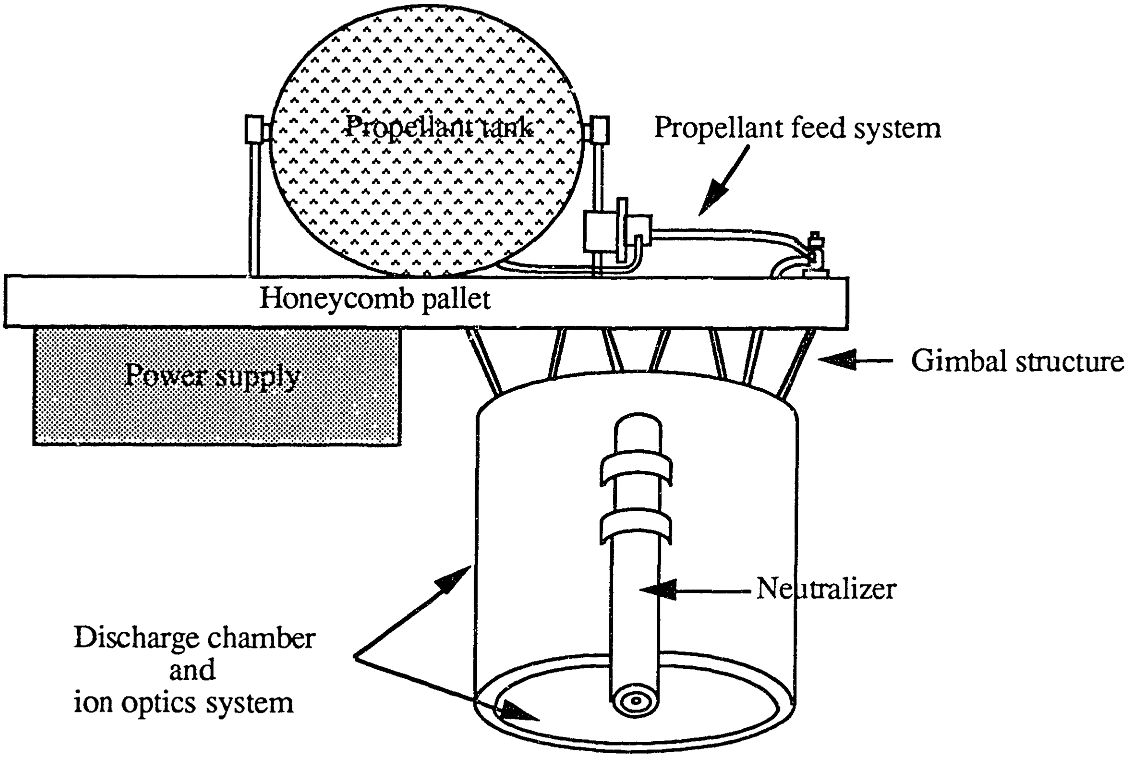

Figure 1.1. State of the art ion propulsion system [5].

In the 1960's and 1970's a divergent magnetic field configuration, such as those found in the J-series ion engines, was widely used. However, with the introduction of the ring-cusp magnetic configuration in the early 1980's, divergent field engines have almost disappeared, because the ring cusp thrusters offered significantly better performance due to a larger ion production region. In a ring cusp thruster, the magnetic field is created by a series of rings of magnets of alternating polarity. Figure 3.2 shows typical magnetic cusps found in an ion thruster. These rings are placed along the back and sides of the thruster. The size, strength, and location of these magnets are chosen so as to maximize the ion production region, which is usually taken to be surface determined by the magnetic contour line where the magnitude of the magnetic field is 50 G. Any electron that crosses this surface gets trapped in one of the magnetic cusps underneath the surface. It then travels in a helical path along the cusp eventually striking the magnet where the cusp terminates.

The ideal propellant for an ion thruster would be characterized by a high molecular mass, low first ionization potential, and high electron collision cross-section for first ionization. On the other hand, the cross-sections for second and higher ionizations as well as for excitations should be as small as possible. The first ion thrusters utilized mercury as the propellant gas. Mercury could be stored as a liquid and easily vaporized before entering the chamber. Moreover, mercury was very attractive because of its low first ionization potential, 10.43 eV, and high 2nd and 3rd ionization potentials, 29.2 eV and 63.4 eV [6]. It also had a high molecular mass of 200 amu. However, there were two problems with mercury. Since it was toxic, it was feared that as mercury atoms would exit the spacecraft they could charge exchange with the ambient plasma and return to contaminate the surfaces of the spacecraft. Furthermore, since it had a low boiling temperature, mercury vapor inside the discharge chamber of an ion thruster would condense and contaminate on sensitive surfaces. For mainly these two reasons, all research into mercury ion thrusters was stopped in the early 1980's.

The search for a propellant gas that could provide a better performance than mercury without incurring all of its disadvantages was then begun. At the time, noble gases appeared to be a natural choice. They were heavy and non-toxic. Xenon is not only the heaviest of all noble gases that occur naturally, but it is also the easiest to ionize. Its ionization potential is 12.3 eV, which is larger than mercury's but lower than that of the other noble gases. The performance of a xenon ion thruster is comparable to that of a mercury thruster. However, the high cost of xenon has led researchers to consider other noble gases.

Argon has an ionization potential of 15.8 eV and an atomic mass which is half that of xenon's. Although argon is much cheaper to obtain than xenon, ion thrusters using argon are difficult to operate and offer a performance that is considerably worse than that obtained using xenon. The same statement can be made for the noble gas neon [7]. Even though xenon is very expensive, it is still the most preferred gas for ion propulsion because of the performance offered and its non-toxicity. Nevertheless, the search for a better propellant still continues.

Section 1.3. Buckminsterfullerene

Up to 1985, it was thought that carbon occurred naturally in only two forms, graphite and diamond. However, Kroto et al. [8] discovered the occurrence of clusters of carbon atoms ranging from 30 to 300 carbon atoms arranged symmetrically in a spherical shell. The most common and stable of these clusters consists of 60 carbon atoms arranged in pentagons in a soccer ball-liked shell. Furthermore, the shell is very strong and extremely hard to break apart. Because of its resemblance to the geodesic domes of Buckminster Fuller, this new form of carbon was nicknamed "buckminstefullerene" or "buckeyball." Its molecular structure is presented in Figure 1.2.

The properties of carbon 60 offer significant performance benefits for ion propulsion. It has a low ionization potential, high ionization cross-section by electron collision, and a large molecular mass. Table 1.1 on the next page compares the properties of carbon 60 with substances that have been considered previously for propellants in ion thrusters. Furthermore, since C_{60} was discovered so recently, there has not yet been a thorough assessment of its toxicity.

The use of buckminsterfullerene as a propellant for ion thrusters was first proposed by Leifer et al. [9]. Since her paper was published, more properties of C_{60}, such as the ionization cross-section by collision with electrons, have been measured. These measurements allow a more quantitative theoretical investigation of the performance that would be obtained in an ion thruster using C_{60} for the propellant.

This thesis is divided into into four parts. Chapter II introduces the theory that was used to model the ion thruster. In Chapter III the theory is applied to an ion thruster using xenon in order to verify the results with previous experimental measurements. In Chapter IV the theory is then applied to an ion thruster using C_{60} as the propellant gas. Finally, Chapter V presents a comparison between the performance of a C_{60} ion thruster and other competing electric propulsion technologies, as well as some of the problems that may have to be overcome in order to run an ion thruster with buckminsterfullerene.

Table 1.1. Propellant candidates for ion propulsion.

Property	Propellant			
	Hg	Ar	Xe	C_{60}
1st ionization potential (eV)	10.43	15.8	12.13	7.61
2nd ionization potential (eV)	29.2	27.6	33.3	10.75
1st excitation potential (eV)	4.8	11.7	8.39	2.85
Maximum ionization cross-section (10^{16} cm^{2})	7.03	2.85	5.45	68.2
Atomic mass (amu)	200.59	39.9	131.3	720.11
Cost	Moderate	Low	High	High
Toxicity	High	None	None	None yet

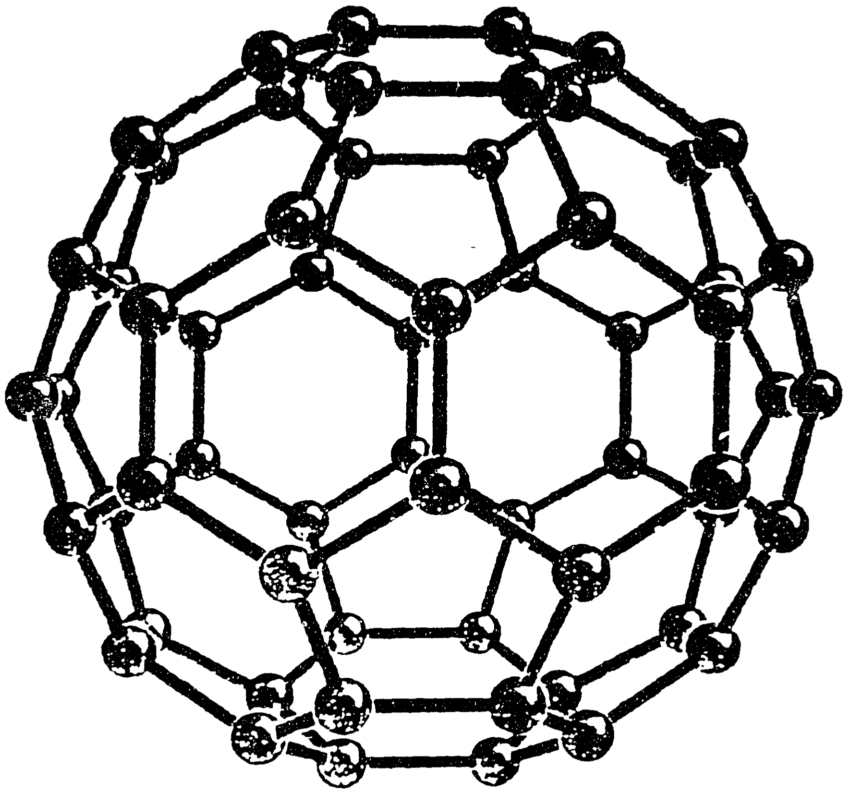

Figure 1.2. Molecular structure of buckminsterfullerene (C_{60}) [10].

Chapter 2. Development of Brophy's Model

In order to characterize the performance of an ion thruster, it is necessary to use a model that takes into account the processes occurring inside it. Different models such as those by Matossian et al. [11], Longhurst et al. [12], etc. have been developed in the past. However, their extensive use of plasma probe measurements render them impractical when the same experimental measurements cannot be performed. A relatively simple and accurate model was developed by Brophy [13] for high flux, low pressure, cusped magnetic field thrusters. One drawback of this model is that it also relies on experimental measurements of certain parameters. However, these parameters depend largely on the geometry and the magnetic field configuration and hence can be taken to be constants for a given thruster. Even though the model cannot predict the performance of a completely new thruster design, it can predict the performance, for different operating conditions or types of propellant, of a thruster where these key parameters have been obtained.

The model is formulated in terms of the average energy required to produce an ion inside the discharge chamber and the fraction of ions that are extracted to form the beam or collected by the surfaces at cathode potential. It predicts the power required to produce 1 A of beam current at different propellant utilization efficiencies, which is more commonly referred to as the "performance curve" of the thruster. Furthermore, the model assumes that the plasma inside the chamber is uniform, with boundaries at the inside walls of the chamber. It also takes the temperatures, densities, and other physical parameters to be constant or given a value averaged over the volume of the discharge chamber.

The model further assumes that the electrons inside the discharge chamber are divided into two groups, primary and secondary, characterized by two different distributions in energy. The primary electrons are those electrons emitted by the hollow cathode that have not undergone any inelastic collisions. They are characterized by a mono-energetic energy distribution. On the other hand, the secondary electrons consist of the primary electrons that have undergone one or more inelastic collisions as well as those electrons liberated in the ionization of propellant atoms. The energy distribution of the secondary electrons can be approximated by a Maxwellian distribution, and thus they are also referred to as Maxwellian electrons. Finally, these two groups of electrons can coexist in the discharge chamber because of the small collision frequencies between the electrons of the two groups [14].

Section 2.1. Definition of Performance

In order to arrive at a measure that describes the performance of an ion thruster, one must account for the power used by its different parts. Figure 2.1 on the next page shows the different power supplies used in a typical ion thruster.

Ground is usually taken to be the body of the spacecraft or the steel structure of the vacuum chamber used in laboratory experiments. The screen grid and the structure of the hollow cathode are biased to a positive V_S volts with respect to ground. The potential of the accelerated beam is approximately determined by that of the neutralizer, which injects electrons to ensure overall thruster neutrality. The neutralizer potential is close to the

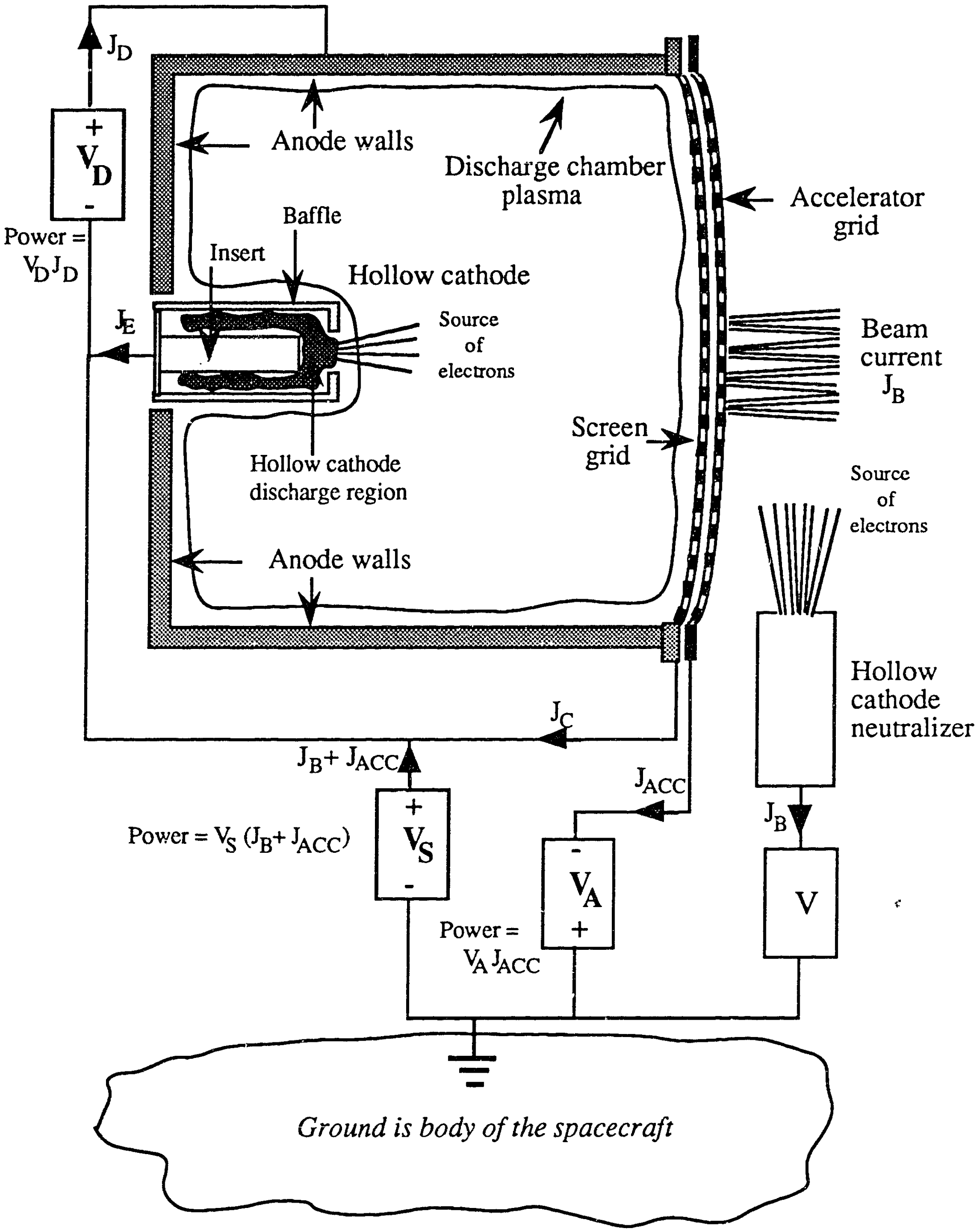

Figure 2.1. Ion thruster with power supplies.

ground potential or, more importantly, to the potential of the background plasma. In Figure 2.1, the neutralizer potential has been taken to be some value V. The walls of the anode are then raised V_D volts above the hollow cathode potential. The power needed to maintain the potential difference between the anode and the cathode is given by $J_D V_D$, where J_D is the current that is evacuated by anode walls. It is usually referred to as the discharge current, and it is composed of the electrons and ions that strike the walls of the anode. Furthermore, the accelerator grid is biased V_A volts negative of ground potential. Some ions, hopefully not many, strike this grid, and hence the power needed to keep the grid at this specified potential is given by $J_{ACC}(V_A + V_S)$, where J_{ACC} is the current of ions collected by the accelerator grid.

The potential profiles found in a typical ion thruster are sketched in Figure 2.2 on the next page. As shown in Figure 2.2a, the potential difference between the anode and cathode surfaces is given by V_D. The plasma within the discharge chamber lies at a potential a few volts more positive than $V_D + V_S$, and this small potential difference is denoted by ΔV_A. Furthermore, the plasma in the region between the insert and baffle of the hollow cathode sits at a potential V_C volts positive with respect to the hollow cathode surfaces. This region is referred to as the hollow cathode discharge region, and it occurs as a result of the power applied to operate the cathode. Electrons are emitted into the discharge chamber from this region, and they are hence accelerated only though a potential difference of $V_D - V_C$ into the chamber.

The potential profile across the ion optics system is presented in Figure 2.2b. The electric field set up across the grids penetrates slightly into the discharge chamber region. Ions that wander into these protrusions of the field are extracted and accelerated through a

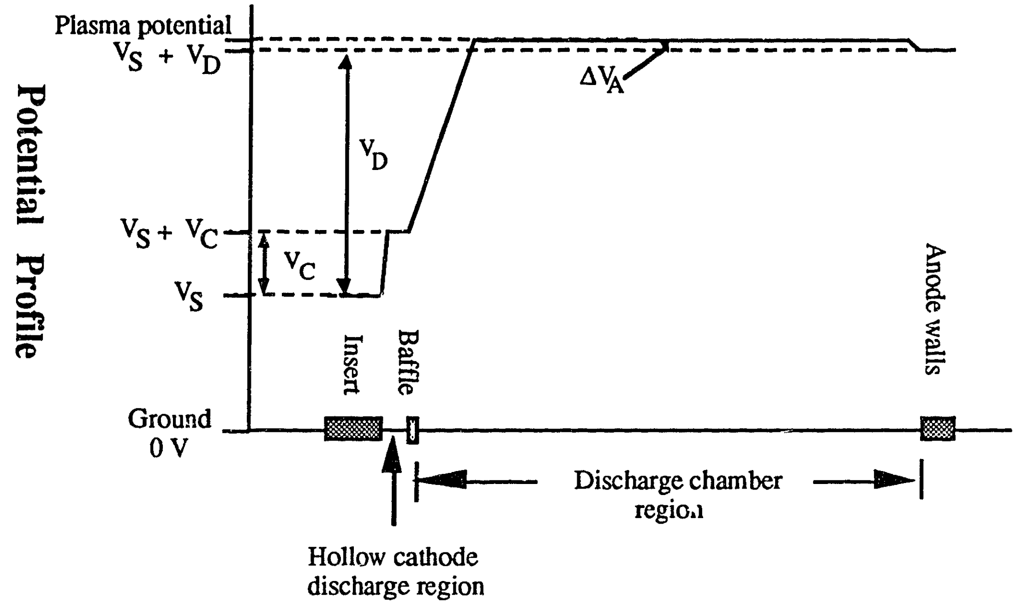

a. Potential profile between anode and cathode potential surfaces.

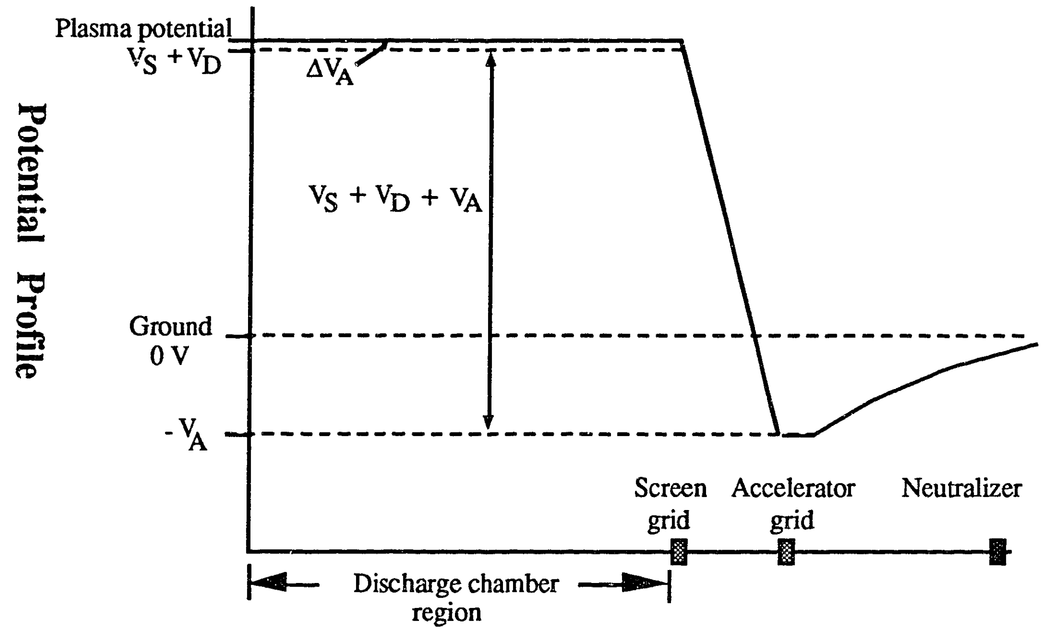

b. Potential profile across ion optics system.

Figure 2.2. Potential profiles of a typical ion thruster.

potential difference $V_S + V_A + V_D$ volts to form a beam of current J_B. After these ions leave the spacecraft, they combine with electrons emitted from the neutralizer to form a quasi-neutral plasma.

From the potential profiles presented, it is reasonable to assume that electrons are collected only by surfaces at anode potential, since the difference between plasma potential and anode potential is negligible. Electrons which make their way to surfaces at cathode potential, such as the hollow cathode structure and screen grid, are repelled back into the discharge chamber because of the strong electric fields caused by the sharp drop in voltage. On the other hand, ions are collected by surfaces both at cathode and anode potential. Each of these ions recombines with an electron from the surface and returns to the discharge chamber as a neutral atom.

The total power used to operate an ion thruster is given by sum of the discharge power ($J_D V_D$), neutralizing power ($J_B V_S$), and the accelerator grid power ($J_{ACC}(V_S + V_A)$). Furthermore, the amount $J_B(V_S + V_D)$ of this total input power is used to accelerate the ions to form a beam. Therefore, the power used to create the beam ions inside the discharge chamber is given by

$$J_B V_S + J_D V_D + J_{ACC}(V_S + V_A) - J_B(V_S + V_D) .$$

One can then define a measure of performance called the beam ion production cost equal to

$$\varepsilon_B = \frac{J_B V_S + J_D V_D + J_{ACC}(V_S + V_A) - J_B(V_S + V_D)}{J_B} ,$$

which represents the power needed to produce a current of 1 A of beam ions. From Figure 2.1, the discharge current is given by the sum $J_E + J_B + J_C + J_{ACC}$, where J_C is the current of ions that strike the cathode potential surfaces and J_E is the electron current emitted by the hollow cathode. Hence, one can rewrite the previous expression as

$$\varepsilon_B = \frac{J_E V_D + J_C V_D + J_{ACC}(V_S + V_A + V_D)}{J_B} ,$$

where the term $J_E V_D$ in the numerator represents the power used to accelerate the primary electrons and the other terms power losses duc ions striking the walls or accelerator grid.

Using the term $J_E V_D$ one can then define another measure of performance called the plasma ion energy cost ε_p taken to be

$$\varepsilon_p = \frac{J_E V_D}{J_P} ,$$

where J_P is the rate of ion production inside the chamber. Thus, the beam ion production cost can be expressed as

$$\varepsilon_B = \frac{J_E V_D}{J_P}\left(\frac{J_P}{J_B}\right) + \frac{J_C V_D}{J_B} + \frac{J_{ACC}(V_D + V_S + V_A)}{J_B} .$$

In the steady state operation of an ion thruster, there is no net accumulation of ions inside the discharge chamber. Therefore, the total ion current produced (J_P) inside the plasma of the chamber must be equal to the total ion current leaving the plasma. From the previous potential profiles, ions can only leave the plasma by falling into cathode potential surfaces, striking anode potential surfaces or accelerator grid, or becoming beam ions. Therefore, the ion production rate must be equal to

$$J_P = J_A + J_B + J_C + J_{ACC},$$

where J_A is the current of ions that strike surfaces at anode potential. Dividing this equation by J_P yields

$$f_A + f_B + f_C + f_{ACC} = 1,$$

where f_A, f_B, f_C, and f_{ACC} refer to the ion fractions J_A/J_P, J_B/J_P, J_C/J_P, and J_{ACC}/J_P, respectively. These fractions of ions depend mostly upon the geometry and the magnetic field configuration of the thruster. Hence, for a family of geometrically similar thrusters, they can be taken to be independent of the mass flow rate, discharge voltage, and the type of propellant gas without incurring significant errors [15]. The similarity should include the primary electron Larmor radius r_L, i.e. r_L/l = constant or $\sqrt{V_D} / Bl$ = constant where l is a characteristic dimension of the thruster and B is a measure of the magnetic field. Inserting these fractions into the expression for the plasma ion energy cost, one obtains

$$\varepsilon_B = \frac{\varepsilon_P}{f_B} + \frac{f_C}{f_B} V_D + \frac{f_{ACC}}{f_B}(V_S + V_A + V_D).$$

Since the fraction of ions collected by the accelerator grid is much smaller than f_A, f_B, or f_C, one can neglect f_{ACC}, and arrive at a useful expression for the beam ion production cost. Namely,

$$\varepsilon_B = \frac{\varepsilon_P}{f_B} + \frac{f_C}{f_B} V_D . \tag{2.1}$$

This expression clearly separates the dependence of the beam ion production cost on the different thruster parameters. In order to predict the performance curve of an ion thruster, the parameters f_B and f_C must be determined for that specific thruster, and the plasma ion energy cost must be calculated as a function of the propellant utilization efficiency for the thruster and the type of propellant used.

Section 2.2. Plasma Ion Energy Cost

The plasma ion energy cost ε_p can be interpreted to be the power used by the thruster inside the discharge chamber to produce a current of 1 A of ions. Equivalently, it can also be taken to be the energy required to produce an ion inside the chamber. Consider a thruster where there are no losses of the primary electrons to the anode walls. In such a case, the plasma ion energy cost will be given the value ε_p^*. This value is usually referred to as the baseline plasma ion energy cost.

Now consider the same thruster where a fraction β of primary electrons are lost to the anode walls. The plasma ion energy cost is then given by

$$\varepsilon_p = \frac{\varepsilon_p^*}{1 - \beta} . \tag{2.2}$$

The cost of producing an ion inside the discharge chamber increases by a factor $1/(1-\beta)$, since more primary electrons must now be used to produce the same number of ions. By knowing β and ε_p^* one can calculate the plasma ion energy cost and then the beam ion production cost.

Reference [13] defines this fraction β through a so called "survival equation." Brophy takes it to be

$$\beta = \exp (\sigma_{t,p} n_o l_e) ,$$

where $\sigma_{t,p}$ is the total inelastic electron collision cross-section of the propellant gas, l_e is primary electron containment length, and n_o is the density of neutrals inside the chamber. The primary electron containment length is defined by Brophy to be the length of the helical path that a primary electron would traverse in the discharge chamber before being collected by the anode, assuming that it had no inelastic collisions through its travel. Hence l_e, by definition, depends only on the geometry and magnetic field configuration of the thruster and the discharge voltage. It does not depend on the propellant type, mass flow rate, propellant utilization, etc. Therefore, it follows that ε_p^* should depend mostly on the type of propellant used and the operating conditions of the discharge chamber.

An expression for the baseline plasma ion energy cost will be derived intuitively by taking into account all possible uses for power inside the discharge chamber. Consider a thruster with no losses inside the discharge chamber. In other words, the primary electrons are accelerated through a potential difference V_D. No excitations of the atomic or ionic states of the propellant atoms or ions occur. No Maxwellian electrons are lost to the anode walls, and no doubly-charged ions are produced. In this case, the electrons just ionize the propellant atoms, whose ionization threshold energy will be taken to be U_+. Furthermore, each ionization event liberates a Maxwellian electron with a thermal energy given by ε_M, which is eventually lost when this Maxwellian electron is collected by the anode. Therefore, the baseline plasma ion energy cost must be given by

$$\varepsilon_p^* = U_+ + \varepsilon_M .$$

However, for most propellant gases the electrons not only ionize the propellant atoms, but also excite them, and the excitation energy is almost immediately radiated away. By taking U_j to be the excitation energy of the jth energy level of a propellant atom, the baseline plasma ion energy cost increases to

$$\varepsilon_p^* = U_+ + \sum_{\substack{j \\ \text{atomic states}}} \alpha_j U_j + \varepsilon_M ,$$

where the coefficients α_j represent the number of excitation events into state j for each ionization event. These coefficients are just the ratio of the excitation rate coefficient into the state j to the ionization rate coefficient, i.e. $<\sigma_j v_e> / <\sigma_+ v_e>$ where these terms are the product of the respective cross-section and the electron velocity averaged over the entire electron energy distribution. The baseline plasma ion energy cost increases, since more energy is now needed to produce an ion because more energy is lost.

In real life thrusters do experience significant losses inside their discharge chambers. Let us take into account that the primary electrons are emitted from the hollow cathode discharge region which is at a potential V_C higher than the surfaces at cathode potential. Since the plasma potential is about $V_D + V_S$, the electrons are only accelerated through a potential difference $V_D - V_C$, and the fraction of energy supplied by the applied discharge voltage that is not used to accelerate the electrons is V_C/V_D. This fraction of energy is lost to the hollow cathode discharge region from where the electrons are emitted. Therefore, the baseline plasma ion energy cost becomes

$$\varepsilon_p^* = \frac{U_+ + \sum\limits_{\substack{j \\ \text{atomic states}}} \frac{\langle \sigma_j v_e \rangle}{\langle \sigma_+ v_e \rangle} U_j + \varepsilon_M}{\left[1 - \frac{V_C}{V_D}\right]},$$

since for the same amount of applied discharge voltage (V_D), a smaller voltage ($V_D - V_C$) is actually available to provide $U_+ + \Sigma\, \alpha_j U_j + \varepsilon_M$.

Finally, taking into account the loss of Maxwellian electrons to the walls of the anode, the baseline plasma ion energy cost is given by

$$\varepsilon_p^* = \frac{U_+ + \sum\limits_{\substack{j \\ \text{atomic states}}} \frac{\langle \sigma_j v_e \rangle}{\langle \sigma_+ v_e \rangle} U_j + \varepsilon_M}{\left[1 - \frac{V_C + \varepsilon_M}{V_D}\right]} . \tag{2.3}$$

The term ε_M appears in the denominator because every primary electron that becomes a Maxwellian electron goes to the anode, and hence a fraction ε_M/V_D of the applied power is lost and never recuperated.

The energy ε_M with which Maxwellian electrons strike the walls of the anode can be related to the electron temperature T_e. Divergilio et al. [16] present this energy as

$$\varepsilon_M = 2\,T_A + \Delta V_A ,$$

where T_A is the electron temperature at the anode and ΔV_A is the difference between plasma potential and anode potential. Brophy and Wilbur take T_A to to be 2/3 T_e and ΔV_A to be 2 V based on their previous experimental work [17]. This could be done better. The rate of electron loss to the anode is

$$\frac{n_M \overline{c_e}}{4} \exp\left(-\frac{V_A}{T_A}\right) A_A ,$$

where A_A is the surface area of the anode, and $\overline{c_e}$ is the mean speed of the Maxwellian electrons. Equating this quantity to J_A should give ΔV_A. However, this calculation would complicate the model, and the results do not depend much on ΔV_A.

Since the plasma inside an ion thruster is characterized by an electron population with two non-interacting energy distributions, a Maxwellian and a mono-energetic one, the previous expression for ε_p^* can be rewritten as

$$\varepsilon_p^* = \frac{U_+ + \displaystyle\sum_{\substack{j \\ \text{atomic states}}} \left[\frac{\frac{n_P}{n_M}\,\sigma_{j,P}\,v_P + \langle \sigma_j\, v_e \rangle_M}{\frac{n_P}{n_M}\,\sigma_{+,P}\,v_P + \langle \sigma_+\, v_e \rangle_M} \right] U_j + \varepsilon_M}{1 - \dfrac{V_C + \varepsilon_M}{V_D}} \, ,$$

where n_P/n_M is the ratio of density of primary electrons to that of Maxwellians in the chamber; $<\sigma_j v_e>_M$, and $<\sigma_+ v_e>_M$ are the excitation rate coefficient and ionization rate coefficient for Maxwellian electrons; and $\sigma_{j,p}$ and $\sigma_{+,p}$ are the exctiation and ionization cross-sections at the primary electron energy. As Brophy notes, the terms under the summation sign may be approximated by considering only a single equivalent lumped excited state characterized by a total excitation collision cross-section σ_{exc} and a lumped excitation energy U_{ex}. This latter parameter is given by

$$U_{ex} = \frac{1}{2}(U_1 + U_+),$$

where U_l is the energy required to excite the lowest energy level. Finally, using Brophy's lumped excitation energy, one obtains a practical expression for the baseline plasma ion energy cost,

$$\varepsilon_p^* = \frac{U_+ + \varepsilon_M + \dfrac{\left[\frac{n_P}{n_M}\,\sigma_{exc,p}\,v_P + \langle \sigma_{exc}\,v_e \rangle_M\right]}{\left[\frac{n_P}{n_M}\,\sigma_{+,p}\,v_P + \langle \sigma_+\,v_e \rangle_M\right]}\,U_{ex}}{1 - \dfrac{V_C + \varepsilon_M}{V_D}} \; . \qquad (2.4)$$

The previous expression for the baseline plasma ion energy cost was obtained by considering the possible uses for the power delivered into the discharge chamber by the primary electrons. No mention was given of where this power comes from. This shows up in the expression for ε_p^* as an inability to calculate the baseline plasma ion energy cost directly. In other words, the thermal energy and the rate coefficients of the Maxwellian electrons depend on the electron temperature. Intuitively, one can understand why the electron temperature and the ratio of the density of primary to Maxwellian electrons in the chamber are not independent of each other. A higher electron temperature causes the Maxwellian electrons to become more mobile around the chamber, and hence they are lost to the anode walls in larger numbers decreasing their density in the chamber. Therefore, one cannot pick the electron temperature and the density of primary to Maxwellian electrons arbitrarily.

In order to calculate the baseline plasma ion energy cost directly, one must not only take into account the uses of the power delivered into the chamber by the primary electrons, but also where this power comes from. The baseline plasma ion energy cost can be written as

$$\varepsilon_p^* = (1 - \beta)\, \varepsilon_p ,$$

and recognizing that the energy of the electrons comes from the applied discharge voltage through the definition of ε_p, one obtains

$$\varepsilon_p^* = (1 - \beta)\, \frac{J_E V_D}{J_P} .$$

The factor $(1 - \beta)$ is the fraction of all primaries which undergo inelastic collisions, and hence

$$(1 - \beta)\, J_E = J_{+,p} + J_{exc,p} = J_{+,p} \left(\frac{J_{+,p} + J_{exc,p}}{J_{+,p}} \right) ,$$

where $J_{+,p}$ and $J_{exc,p}$ are the rates of ionization and excitation of propellant atoms by the primary electrons, respectively. These rates are related to the electron collision cross-sections, and thus one can write the quantity in parenthesis as

$$\frac{J_{+,p} + J_{exc,p}}{J_{+,p}} = \frac{\sigma_{t,p}}{\sigma_{+,p}} ,$$

where $\sigma_{+,p}$ refers to the ionization cross-section of the propellant atoms at the primary electron energy by collisions with electrons and $\sigma_{t,p}$ refers to the total inelastic collision cross-section, which includes both ionization and excitation. In other words, $\sigma_{t,p}$ is equal to $\sigma_{+,p} + \Sigma\, \sigma_{j,p}$, where $\sigma_{j,p}$ is the collision cross-section for the excitation of the jth energy level. Inserting this quantity into the expression for the baseline plasma ion energy cost, one obtains

$$\varepsilon_p^* = \frac{J_{+,p}}{J_P} \frac{\sigma_{t,p}}{\sigma_{+,p}} V_D \; . \tag{2.5}$$

One can relate the ratio of the ion production rate by primaries to the total ion production rate to the ionization rate coefficients and densities of primary and Maxwellian electrons. In other words,

$$\frac{J_{+,p}}{J_P} = \frac{J_{+,p}}{J_{+,p} + J_{exc,p}} = \frac{1}{1 + \dfrac{n_M}{n_P} \dfrac{\langle \sigma_+ v_e \rangle_M}{\sigma_{+,p} v_P}} \; .$$

Using this ratio, one can arrive at a second expression for the baseline plasma ion energy cost. Namely,

$$\varepsilon_p^* = \left(\frac{\sigma_{t,p}}{\sigma_{+,p}} V_D \right) \left(\frac{1}{1 + \dfrac{n_M}{n_P} \dfrac{\langle \sigma_+ v_e \rangle_M}{\sigma_{+,p} v_P}} \right) \; . \tag{2.6}$$

These two expressions can be solved simultaneously for the baseline plasma ion energy cost. The values obtained for ε_p^* can then be entered into Eq. (2.3) in order to calculate the plasma ion energy cost. This intuitive approach explains the meaning of the two expressions for the baseline plasma ion energy cost which were originally presented in Reference [13].

Section 2.3. Calculation of the Baseline Plasma Ion Energy Cost

In order to calculate the ε_p^* for a propellant gas, Eqs. (2.4) and Eq (2.6) must be solved simultaneously for the baseline plasma ion energy cost, electron temperature, and the ratio of the density of primary to Maxwellian electrons. The solution is a three-dimensional surface that relates these three quantities. In order to obtain such a surface, Eqs. (2.4) and (2.6) will be plotted versus the electron temperature for a constant ratio of primary to Maxwellian electrons. Figure 2.3a on page 41 presents two typical curves, in which the ratio n_P/n_M has been taken to be some number C_3.

The ratio of the density of primary to Maxwellian electrons depends on the electron temperature. As the electron temperature increases, this ratio also increases. Therefore, not all of the points in the two curves are solutions. Only the intersection of the two curves, the equilibrium point, is a solution and it represents physical parameters. In order to motivate this reasoning, consider again the two curves in Figure 2.3a Now pick an electron temperature T_1 that is lower than the equilibrium electron temperature T_e. At this lower temperature and the given ratio of primary to Maxwellian electrons, the contribution of the Maxwellian electrons to the ionization process is less. Therefore, more energy transferred from the primaries to the Maxwellians is lost, and Eq. (2.6) predicts a higher baseline plasma ion production cost. However, at this lower electron temperature, fewer Maxwellian electrons are being collected by the anode. Eq. (2.4) says that the baseline plasma ion energy cost should be less, because there are fewer losses of the power input into the chamber by the primary electrons. We can now ask what has happen to the energy transferred from the primaries to the Maxwellians. It is not being used for ionization, and it is not being lost to the walls of the anode. It must then be used to heat the Maxwellians to increase their temperature to the value at equilibrium. The same reasoning applies in the opposite case, i.e. if the electron temperature were assumed to be a value T_2 higher than the equilibrium value.

Eqs. (2.4) and (2.6) can be plotted again for a different ratio of primary to Maxwellian electrons as shown in Figure 2.3b. A new equilibrium point for the baseline plasma ion energy cost, electron temperature, and ratio of the primaries to Maxwellians is obtained. The process can be repeated many more times to generate the entire three-dimensional solution, but n_P/n_M remains an unknown. We will show in what follows that its value is determined by a specification of the propellant utilization efficiency.

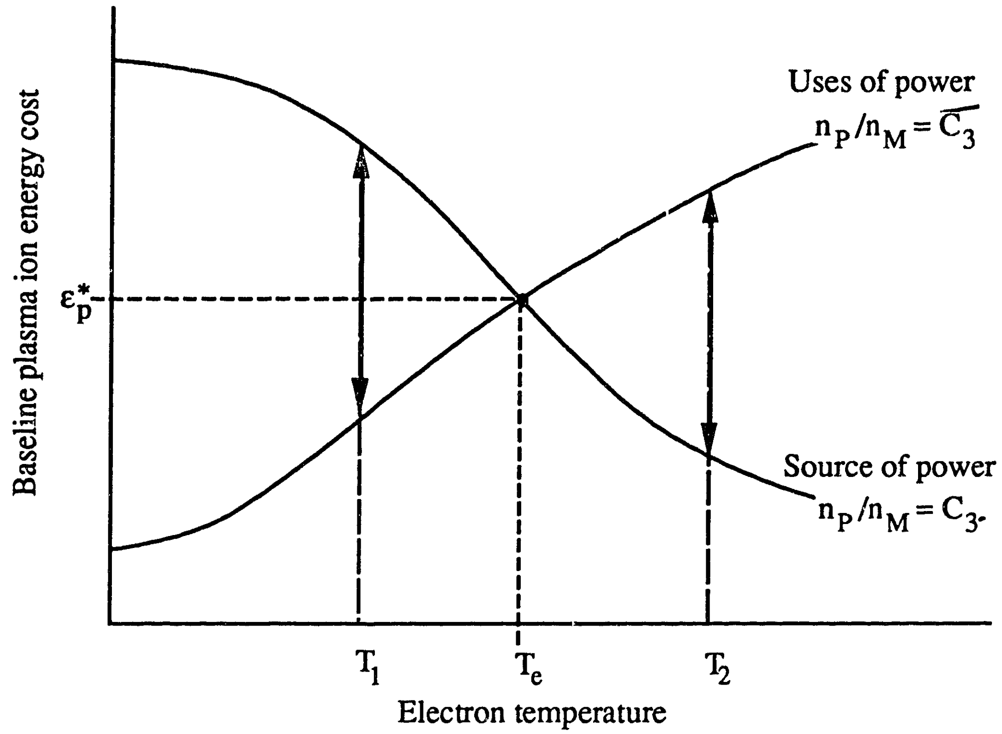

a. Typical curves determined by Eqs. (2.4) and (2.6).

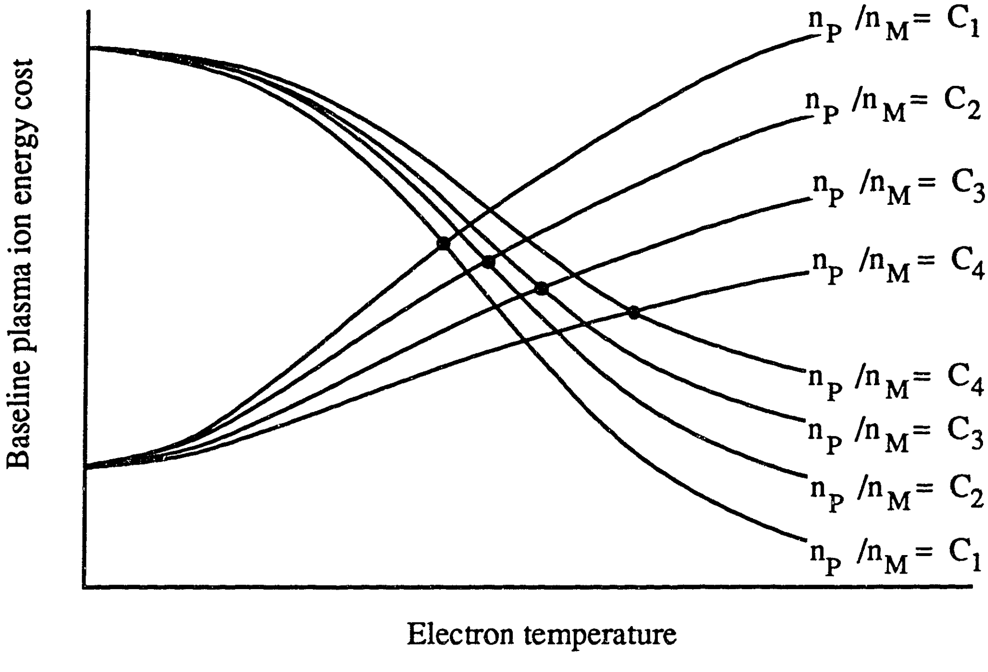

b. Locus of equilibrium points.

Figure 2.3. Baseline plasma ion energy cost.

Section 2.4. Propellant Utilization Efficiency

Each of the equilibrium points obtained in previous section corresponds to a different propellant utilization efficiency. This efficiency is defined through

$$\eta_u = \frac{J_B}{\dot{m}} ,$$

where $\dot{m}$ is the propellant mass flow rate. Using Eq. (2.5) one can relate the propellant utilization efficiency to the baseline plasma ion energy cost, electron temperature, and the ratio of primary to Maxwellian electrons. Using the definition of η_u and f_B one can write Eq. (2.5) as

$$\frac{J_{+,p}}{J_P} = \frac{\varepsilon_p^*}{V_D} \frac{\sigma_{+,p}}{\sigma_{t,p}} ,$$

and, since $J_P = J_B / f_B = \dot{m}\,\eta_u / f_B$,

$$J_{+,p} = \frac{\dot{m}\ \eta_u\ \varepsilon_p^*\ \sigma_{+,p}}{f_B\, V_D\, \sigma_{t,p}} .$$

Furthermore, since $J_{+,p}$ is given by $e\, n_o\, n_P\, \sigma_{+,p}\, v_p\, V$, one can solve for the density n_P of the primary electrons inside the discharge chamber:

$$n_P = \left[\frac{\dot{m}\,\eta_u\,\varepsilon_p^*\,\sigma_{+,p}}{f_B\,V_D\,\sigma_{t,p}}\right]\left[\frac{1}{n_o e\,\sigma_{+,p}\,v_p\,V}\right].$$

This equation depends on the neutral density. Nevertheless, one can express the neutral atom density in terms of the propellant utilization efficiency. By conservation of mass, the propellant mass flow rate must equal

$$\dot{m} = J_B + J_o \ ,$$

where J_o is the rate at which neutrals flow across the grids. Using the theory of free molecular flow through a sharp-edged orifice, this neutral flow rate may be expressed as

$$J_o = \frac{1}{4}\, n_o\, e\, v_o\, A_g\, \phi_o,$$

where A_g is the area of the grids, ϕ_o is the transparency of the grids to neutrals, and v_o is the mean neutral thermal speed.

Therefore, using the previous two equations and the definition of the propellant utilization efficiency, one can write the neutral density inside the thruster as

$$n_o = \frac{4\ (1 - \eta_u)\ \dot{m}}{e\ v_o\ A_g\ \phi_o} . \tag{2.7}$$

Inserting this expression into the equation for the density of primary electrons, one obtains

$$n_P = \left[\frac{\varepsilon_p^* A_g \phi_o v_o}{4\ v_p\ V\ f_B\ V_D\ \sigma_{t,p}} \right] \left[\frac{\eta_u}{1 - \eta_u} \right] .$$

This expression relates the propellant utilization efficiency to the density of primary electrons and the baseline plasma ion energy cost. The goal is to relate it also to the density ratio of primary to Maxwellian electrons.

Since plasmas obey quasi-neutrality, the ion density n_i is equal to the density of electrons, $n_P + n_M$. Therefore, one can relate the ratio of primaries to Maxwellians to the ratio of primaries to ions:

$$\frac{n_P}{n_M} = \frac{n_P}{n_i - n_P} = \frac{\frac{n_P}{n_i}}{1 - \frac{n_P}{n_i}} .$$

One can also relate the average ion density to the beam current by

$$n_i = \frac{J_B}{0.6\, e\, v_b\, A_g\, \phi_i}, \tag{2.8}$$

where v_b is the Bohm velocity and ϕ_i is the transparency of the grids to ions. Therefore, the ratio n_P/n_i becomes

$$\frac{n_P}{n_i} = \left[\frac{0.15\, e\, e_p^*\, v_b\, A_g^2\, \phi_o\, \phi_i\, v_o}{v_p\, V_D\, f_B\, V\, \sigma_{t,p}}\right]\left[\frac{1}{J_B\left(\frac{1}{\eta_u} - 1\right)}\right]. \tag{2.9}$$

Finally, knowing the electron temperature, the ratio of the density of primaries to Maxwellians, and the baseline plasma ion energy cost, one can solve for the corresponding propellant utilization efficiency.

Section 2.5. Performance Curves

Using Brophy's model one was able to break the dependance of the beam ion production cost into parameters that depend on the physical design of the thruster, operating conditions, and/or the type of propellant used. In doing so we arrived at

Eq. (2.1). What remains to be done is to relate the beam ion production to the propellant utilization efficiency, and hence obtain a mathematical model of the performance curves of an ion thruster.

In the previous section, we obtained a relation between plasma ion energy cost and the baseline plasma ion energy cost. Inserting this relation into Eq. (2.1), one arrives at

$$\varepsilon_B = \frac{\varepsilon_p^*}{f_B} \frac{1}{1 - \exp(-n_o \sigma_{t,p} l_e)} + \frac{f_C}{f_B} V_D .$$

Furthermore, in the previous section, we related the baseline plasma ion energy cost to the propellant utilization efficiency. In order to arrive at the performance curves, the exponential term must now be written in terms of η_u.

Using the expression for the density of neutrals inside the discharge chamber presented in Eq. (2.7), the exponential term becomes

$$\exp(-n_o \sigma_{t,p} l_e) = \exp\left(- \frac{4 \sigma_{t,p} l_e}{e v_o A_g \phi_o} (1 - \eta_u) \dot{m} \right).$$

Finally, one arrives at a useful mathematical expression for the performance curve of an ion thruster.

$$\varepsilon_B = \frac{\varepsilon_p^*}{f_B} \frac{1}{1 - \exp(-C_o (1 - \eta_u) \dot{m})} + \frac{f_C}{f_B} V_D , \qquad (2.10)$$

where the parameter C_0 has been taken to be

$$C_o = \frac{4 \sigma_{t,p} l_e}{e \, v_o \, A_g \, \phi_o} .$$

This parameter with dimensions of $\dot{m}^{-1}$, i.e. sec/kg or (Equivalent Ampere)$^{-1}$, depends both on the propellant type and the geometry and magnetic field configuration of the thruster. Since C_0 is proportional to the primary electron containment length, it measures how well the primary electrons are contained in the discharge chamber. Furthermore, since it also depends on the total inelastic collision cross-section of the propellant gas, it also measures how well the propellant gas uses the primary electrons. This is why C_0 is usually referred to as the primary electron utilization factor, since it is a measure of how well the thruster with its propellant gas utilize the primary electrons.

In order to predict the performance of a thruster, one needs to calculate f_B and f_C which only depend on the design of the thruster, ε_p^* which only depends on the type of propellant and the operating conditions, and C_0 which depends on both. Before applying Brophy's model to carbon 60, the model will be applied to a thruster using xenon for the propellant gas in order to verify its overall accuracy.

Chapter 3. Predictions of the Model for Xenon

In order to verify the accuracy of the model developed by Brophy and Wilbur, this model will be first applied to a Hughes 13 cm laboratory-model thruster using xenon as the propellant gas. The predictions of the model for the beam ion production cost will then be compared with the performance measured experimentally for this thruster.

The Hughes 13 cm lab-model thruster is shown in Figure 3.1 on page 50, and it is a thruster used at the Hughes Research Labs primarily for research in ion propulsion. The diameter of the exit area of the discharge chamber is 13 cm, and the thruster is referred to as a lab-model since it was not built to a rigorous set of flight-qualification standards. It was chosen for this research primarily for three reasons. First, its performance using xenon as the propellant gas had been measured experimentally by Beattie et al. [18]. Second, this thruster eventually would be modified to run with carbon 60. Third, since smaller ion thrusters require less power than larger ones, it was sought to determine if a carbon 60 ion thruster would be comparable to other electric propulsion devices, such as the Russian Stationary Plasma Thruster, in terms of the thrust to power ratio. Finally, xenon was used as the propellant gas, since this noble gas appears to be lately the preferred fuel for ion propulsion due to its non-toxicity and large electron ionization collision cross-section relative to other gases.

Even though the 13 cm lab-model thruster is not flight-qualified, its performance is comparable to the one of flight-qualified 13 cm ion thrusters [19]. However, unlike flight -qualified thrusters of similar size, it uses a larger set of grids that were originally intended for a 30 cm ion engine. This is because smaller grids are much more expensive to fabricate. However, the effects of the larger grids on extracting and accelerating ions out the chamber should be negligible, since they fit on the thruster exactly where an appropriate set of smaller grids would.

In order to apply Brophy's model, the operating conditions of the thruster, namely the discharge voltage V_D and the beam current J_B, must first be determined. Then, the parameters C_0, f_B, f_C, ϕ_i, and ϕ_0 must be obtained. Now, the baseline plasma ion energy cost ε_p^* can be calculated using Eqs. (2.4) and (2.6). Finally, the beam ion production cost can be tabulated versus the propellant utilization efficiency and compared with the actual performance measured.

Section 3.1. Primary Electron Utilization Factor

The primary electron utilization factor C_0 measures how efficiently a thruster makes use of the primary electrons. As derived in Chapter 2, it is given mathematically by the expression

$$C_o = \frac{4\,\sigma_t\, p\, l_e}{e\, v_0\, A_g\, \phi_0}\,, \tag{3.1}$$

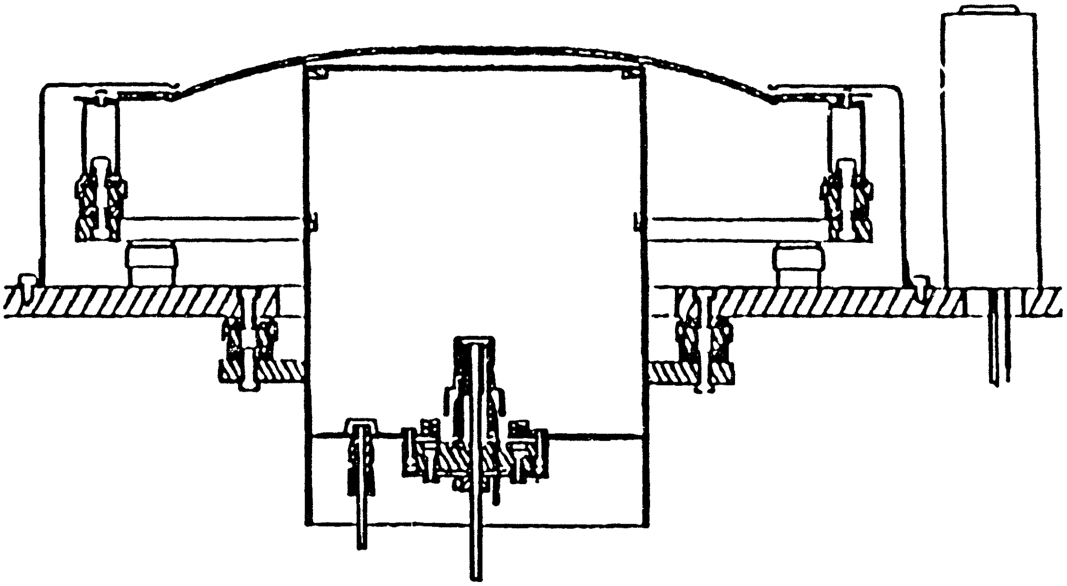

Figure 3.1. Diagram of the Hughes 13 cm laboratory-model thruster [20].

It depends on the geometry and the magnetic field configuration of the thruster through the primary electron containment length. On the other hand, it depends on the type of propellant gas through the inelastic collision cross-sections. Unfortunately, this parameter had not been measured for the Hughes 13 cm lab-model thruster. However, it can be calculated using a set of computer codes developed by Arakawa et al. [21].

The set of codes written by Arakawa can compute the primary electron utilization factor once the collision cross-sections for ionization and excitation of the propellant gas by electrons have been obtained and the physical dimensions of the discharge chamber and the magnets have been measured. These codes have been used in the past to determine C_0 for other thrusters. The results presented in Arakawa and Yamada [22] agree remarkably well with previous experimental measurements. Arakawa's codes consists of two main programs. One program computes the magnetic vector potential inside the thruster and the other tracks the path of primary electrons within this magnetic field.

Magnetic Field Analysis Code

The first program is a finite-element code that calculates the magnetic vector potential inside the discharge chamber of the thruster. The program assumes that the thruster is of the ring-cusp type with cylindrical symmetry. Furthermore, the program requires the locations, dimensions, and permeability of the walls that comprise the discharge chamber of the thruster. It also asks the user for the location, dimensions, and directions of the magnets along the walls of the chamber and the position of the orifice of the hollow cathode inside the thruster. These parameters were measured with a Mituitoyo digital caliper for the Hughes 13 cm lab-model thruster. A schematic of the results are sketched in Figure 3.2 on the next page.

The walls of the thruster were made up of stainless steel, and the magnets used were samarium-cobalt permanent magnets. The direction of the magnets needed for Arakawa's program were taken to be either a +1 or -1 depending on whether the north face of the magnet was pointing along the positive direction defined by the coordinate system used.

These measurements were then entered into Arakawa's finite-element program. In order for the code to know the locations of all parts of the chamber, the spacing between the nodes in the finite-element analysis was taken to be smallest dimension of the smallest part of the thruster. This turned out to be the thickness of the chamber walls, which were measured to be 0.157 cm. Because of the small mesh size used, the program could not be run on an IBM Personal Computer. Instead, the program was modified to run on a UNIX Stardent computer, which could store and manipulate the large arrays of information generated with its plentiful Random Access Memory. The output of the finite-element program was a data array with the locations and components of the magnetic vector potential.

Monte Carlo Simulation for C_o

The values obtained for the magnetic vector potential were then entered into a second program that tracked the trajectories of primary electrons inside the discharge

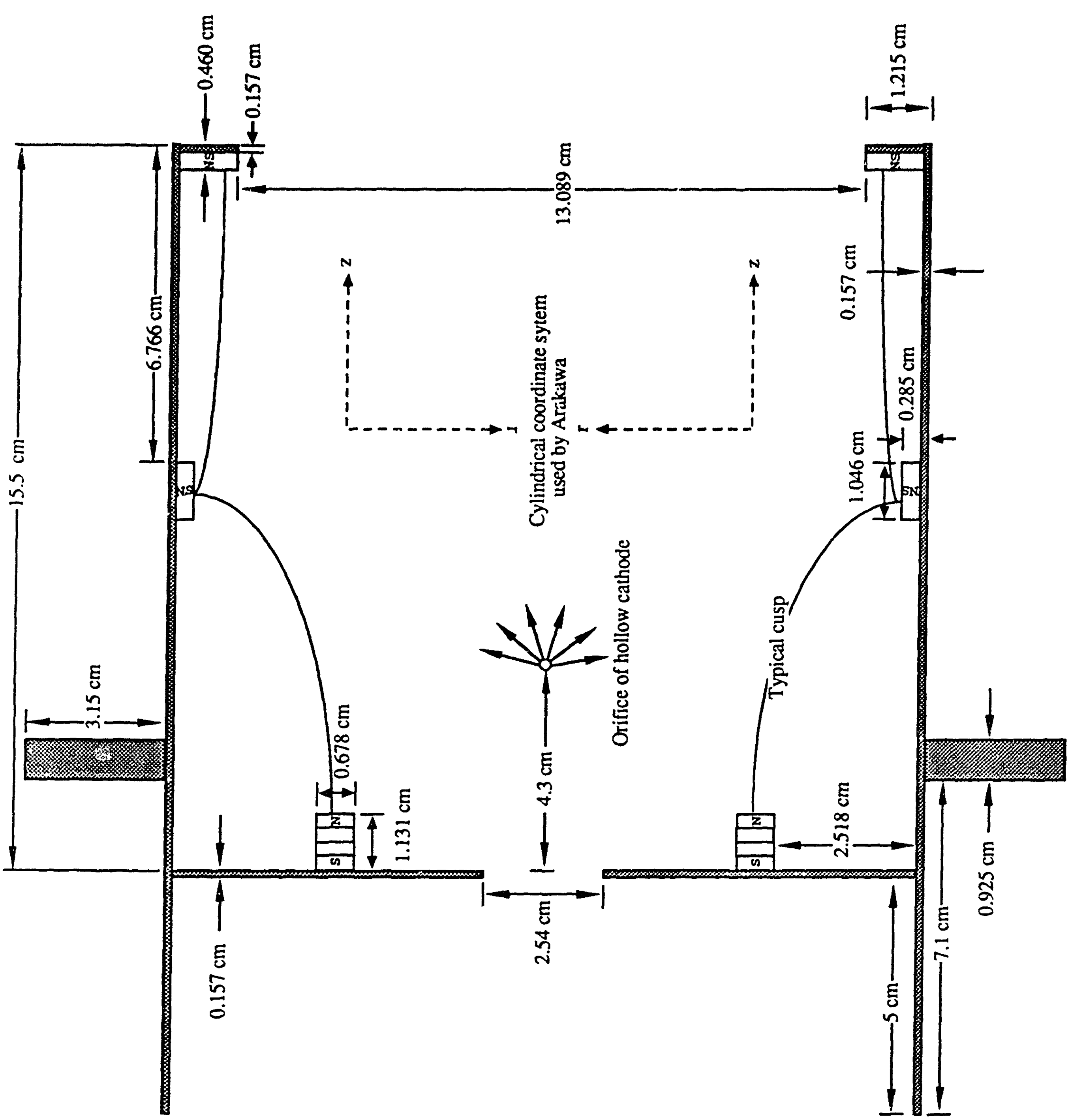

Figure 3.2. Schematic of the discharge chamber of the 13 cm lab-model thruster.

chamber of the thruster. The program uses a Monte Carlo technique in which the position and velocity of the trial electrons are surveyed as a function of time.

The code takes the Lagrangian of a primary electron of mass m and charge e to be

$$L = \frac{1}{2} m |V|^2 - e(\vec{V} \cdot \vec{A}),$$

where $\vec{V}$ is the velocity of the electron and $\vec{A}$ is the magnetic vector potential calculated previously using the magnetic field analysis program. Using the Euler-Lagrange equations on cylindrical coordinates, the program determines the equations of motion.

$$m\frac{dv_r}{dt} = \frac{v_\theta^2}{m\,r} - e\frac{v_\theta}{r}\frac{\partial A_\theta}{\partial r} ,$$

$$m\frac{dv_z}{dt} = - e\frac{v_\theta}{r}\frac{\partial A_\theta}{\partial z} .$$

For each primary electron emitted at the hollow cathode, its trajectory is computed by integrating these equations of motion using a Runge-Kutta method. The integration time step is chosen so that the distance that the electron travels during this time interval is one order of magnitude less than the Larmor radius. Moreover, the value of the Larmor radius varies with the field strength at each position of the electron. When a primary electron reaches any surface at cathode potential, it is reflected back into the chamber due to the sharp drop in the electrostatic potential. However, when it reaches the anode walls, the primary electron is lost. The length that the electron has traversed inside the chamber from the time it emanates from the cathode to the time when it is lost to the anode is then computed and averaged. This length is the primary electron containment length l_e.

The program tracks the trajectories of 1102 electrons, one at a time. Arakawa claims that when the trajectories of 10,000 electrons are computed, the probable error in the value of the primary electron containment length is about 2 %. For 400 electrons the error jumps up to about 10 %. Hence, the error in using 1102 electrons is less than 10 % [23].

Using the values for the magnetic vector potential calculated from the finite-element analysis program, the Monte Carlo simulation was ran 5 times for a discharge voltage of 30 V. The average value of the primary electron utilization factor from these five runs was obtained to be 12.32 A^{-1} for the Hughes 13 cm laboratory-model thruster. This value is in agreement with the previously measured values for similar thrusters. The primary electron utilization factor for a 12 cm thruster was measured experimentally by Vaugh and Wilbur to be 12 A^{-1} using xenon as the propellant gas [24].

Section 3.2. Ion Fractions, f_B and f_C

The fraction of ions extracted into the beam and the fraction of ions collected by surfaces at cathode potential have not been measured for the Hughes 13 cm laboratory model thruster. However, they have been measured for a Hughes 30 cm ring-cusp thruster, which uses a similar design for the discharge chamber. Since the Hughes 30 cm thruster uses the same type of cathode and cathode assembly as the 13 cm lab-model thruster, f_C in the 13 cm thruster to a first approximation was taken to 0.1, which is the same fraction measured for the 30 cm thruster [25]. Although f_C would most likely be higher than 0.1, there was no other way to obtain a better value, other than running the thruster and setting up an experiment to measure it, which was not possible at the time.

Furthermore, the extracted ion fraction f_B was taken to be 0.3 [26]. This is a reasonable assumption since one can relate the extracted ion fraction of the 13 cm thruster to the one of the 30 cm thruster. The beam ion production cost for any thruster is given by

$$\varepsilon_B = \frac{1}{f_B}[\varepsilon_p + f_C V_D] .$$

Using the same propellant gas, operating at the same discharge voltage, and operating at a very low propellant utilization, the term

$$[\varepsilon_p + f_C V_D],$$

should be approximately the same for the 30 cm thruster as for the 13 cm one. At a low propellant utilizations, there are few losses of primary electrons to the anode walls, and hence the magnetic field configuration and physical design of the thruster is not as important. In other words, ε_p equals ε_p^*. Therefore, by taking the ratio of the beam ion production cost of the 30 cm thruster at a discharge voltage of 30 V and a propellant utilization efficiency less than 50 % to the beam ion production cost of the 13 cm lab-model thruster at the same conditions, one obtains an estimate for f_B.

$$\frac{\varepsilon_{B,30\ cm}}{\varepsilon_{B,13\ cm}} = \frac{\frac{1}{f_{B,30\ cm}}\left[\varepsilon_p + f_c V_D\right]}{\frac{1}{f_{B,13\ cm}}\left[\varepsilon_p + f_c V_D\right]} = \frac{f_{B,13\ cm}}{f_{B,30\ cm}} .$$

The extracted ion fraction for the 30 cm thruster has been measured to be 0.5, while the beam ion production cost has been found to be about 90 eV/beam ion at low propellant utilization efficiencies [27]. Since from Reference [18] one can extrapolate the beam ion production cost of the 13 cm laboratory-model thruster to be 160 eV/beam ion at low propellant utilization efficiencies, the extracted ion fraction was computed to be about 0.3.

As a final note, the values for f_B and f_C presented in this section should be taken as approximations of the actual values.

Section 3.3. Transparencies of the Ion Optics System

The ion optics system used in this thruster consists of two grids, a screen grid and an accelerator grid. No decelerator grid was used with this thruster. The dimensions of the holes and the spacings between the grids are shown in the on the next page.

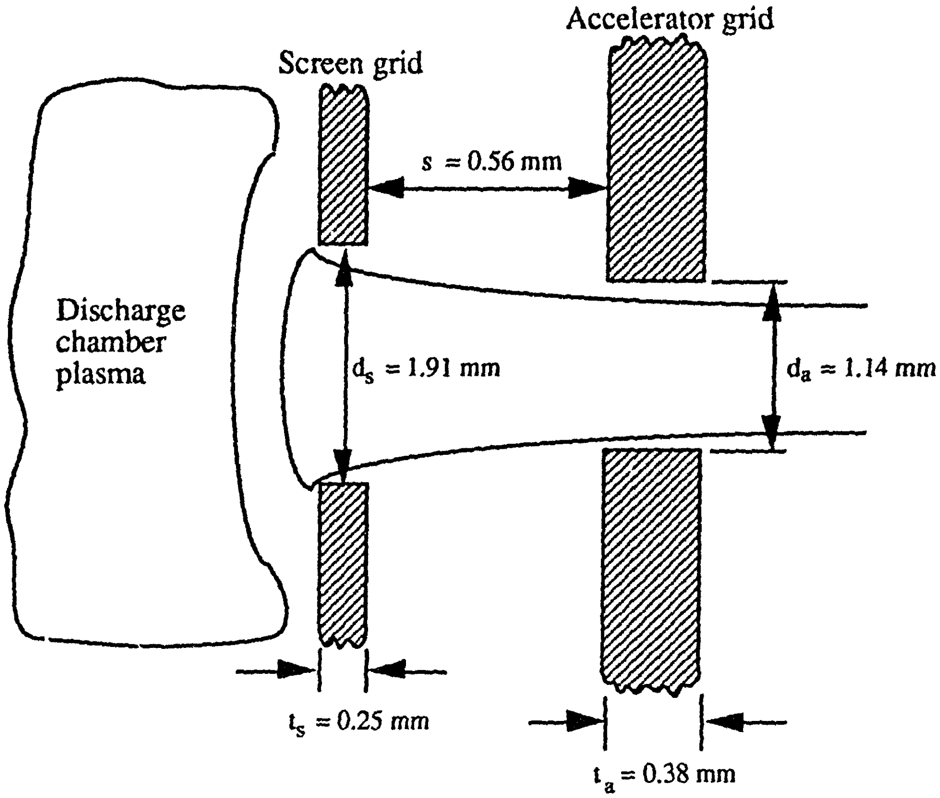

Figure 3.3. Geometry of the ion optics system used.

The transparency of this set of grids to ions ϕ_i has been measured previously by Beattie and Matossian [28]. They measured it to be 81.76 % and relatively insensitive to the thruster operating parameters. Furthermore, the transparencies of the grids to neutrals ϕ_o was found to be 0.167 in the manner described by the previous reference.

Section 3.4. Baseline Plasma Ion Energy Cost

The baseline plasma ion energy cost was calculated in the same manner as described in Chapter 2. The two expressions for ε_p^* are repeated below for convenience.

1. Baseline plasma ion energy cost by uses of power inside the discharge chamber:

$$\varepsilon_p^* = \frac{U_+ + \varepsilon_M + \dfrac{\left[\dfrac{n_P}{n_M}\sigma_{exc,p}v_P + \left\langle\sigma_{exc}v_e\right\rangle_M\right]}{\left[\dfrac{n_P}{n_M}\sigma_{+,p}v_P + \left\langle\sigma_+ v_e\right\rangle_M\right]}U_{ex}}{1 - \dfrac{V_C + \varepsilon_M}{V_D}} . \tag{3.2}$$

2. *Baseline plasma ion energy cost by the source of power:*

$$\varepsilon_p^* = \frac{1}{1 + \dfrac{n_M}{n_P}\dfrac{\left\langle\sigma_+ v_e\right\rangle_M}{\sigma_{+,p}v_P}} \frac{\sigma_{t,p}}{\sigma_{+,p}} V_D. \tag{3.3}$$

In order to find the baseline plasma ion energy cost, electron temperature, and the ratio of the density of primary to Maxwellian electrons, the previous two equations must be solved simultaneously. The discharge voltage V_D was taken to 30 V, since this was the voltage that was used in the experimental measurements of Reference [18]. Furthermore, the ionization and excitation threshold energies of xenon were taken to be 12.1 eV and 8.3 eV, respectively. This implied a lumped excitation energy U_{ex} of 10.2 eV. Moreover, the ionization and excitation collision cross-sections for xenon atoms with electrons were obtained from Rapp and Englander-Golden [29] and Hayashi [30], respectively. These cross-sections are plotted in Figures 3.4. Using these cross-sections, the excitation and ionization rate coefficients by electrons were then computed.

For Maxwellian electrons, the rate coefficients are given by

$$< \sigma v_e > = \frac{\sqrt{\frac{2e}{m}} \int_0^{\infty} \sigma(E)\ E\ e^{-E/T_e}\ dE}{\int_0^{\infty} \sqrt{E}\ e^{-E/T_e}\ dE},$$

where the cross-section σ is the excitation or ionization collision cross-section depending on whether one is interested in the ionization or excitation rate coefficient. In order to compute the rate coefficients, a computer program was first written to calculate a seventh order polynomial fit of the cross-sections. This polynomial fit was then entered into a second program that used a Runge-Kutta method to calculate the integral in the previous expression. Figure 3.5 plots the ionization and excitation rate coefficients computed for xenon as a function of the electron temperature.

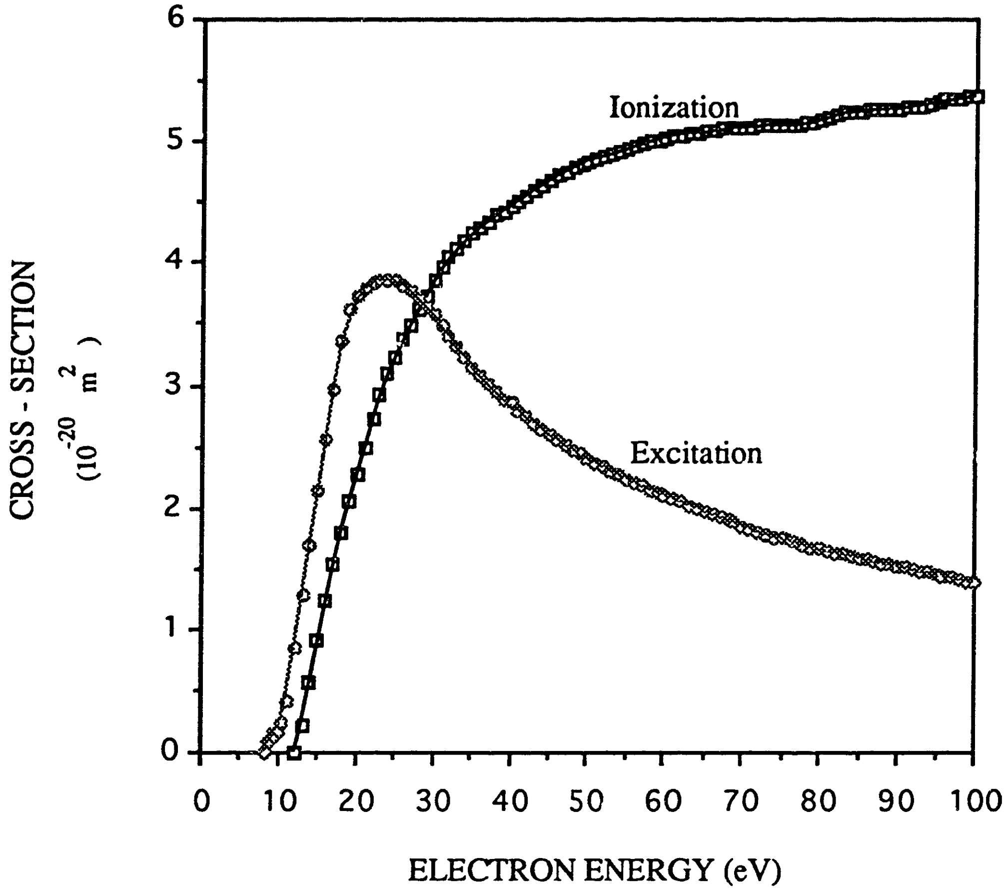

Figure 3.4. Measured collision cross-sections for ionization and excitation of xenon atoms by electrons.

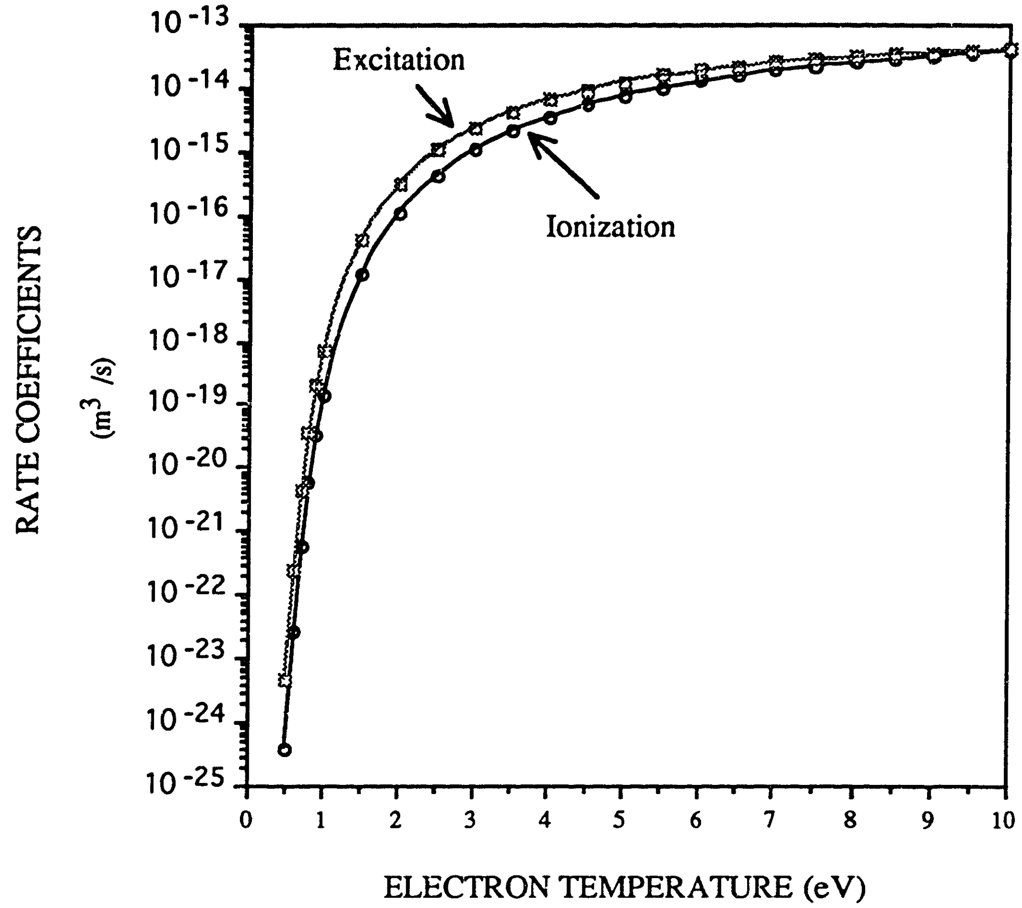

Figure 3.5. Ionization and excitation rate coefficients for collisions between xenon atoms and Maxwellian electrons.

Furthermore, the velocity v_P of the primary electrons was taken to be

$$v_P = \sqrt{\frac{2e\,(V_D - V_C)}{m}}\ ,$$

where V_C is the potential at the surface of the cathode and m is the mass of an electron, $9.1\text{x}10^{-31}$ kg. If the source of primary electrons into the discharge chamber of a thruster happens to be a filament, then V_C is equal to 0 V. However, for a thruster, like the Hughes 13 cm laboratory-model thruster, which operates with a hollow cathode, the value for V_C ranges between 0 V and 10 V. It was found that increasing V_C from 0 V caused the baseline plasma ion energy cost to increase and the electron temperature to decrease. This is expected because as the hollow cathode voltage increases the primary electrons enter the discharge chamber plasma with less energy. Since no one had ever measured this loss for this thruster, V_C was assumed to be 5 V.

Both expressions for the baseline ion energy cost were then plotted versus electron temperature for different ratios (n_P/n_M) of the density of primary to Maxwellian electrons. As shown in Figure 3.6 on the next page, the intersection of the curves provided the equilibrium points that showed which combinations of ε_p^*, T_e, and n_P/n_M could exist inside the discharge chamber of the thruster.

Finally, the propellant utilization efficiency η_u at these equilibrium points was calculated in the manner described in Chapter 2 using the equation,

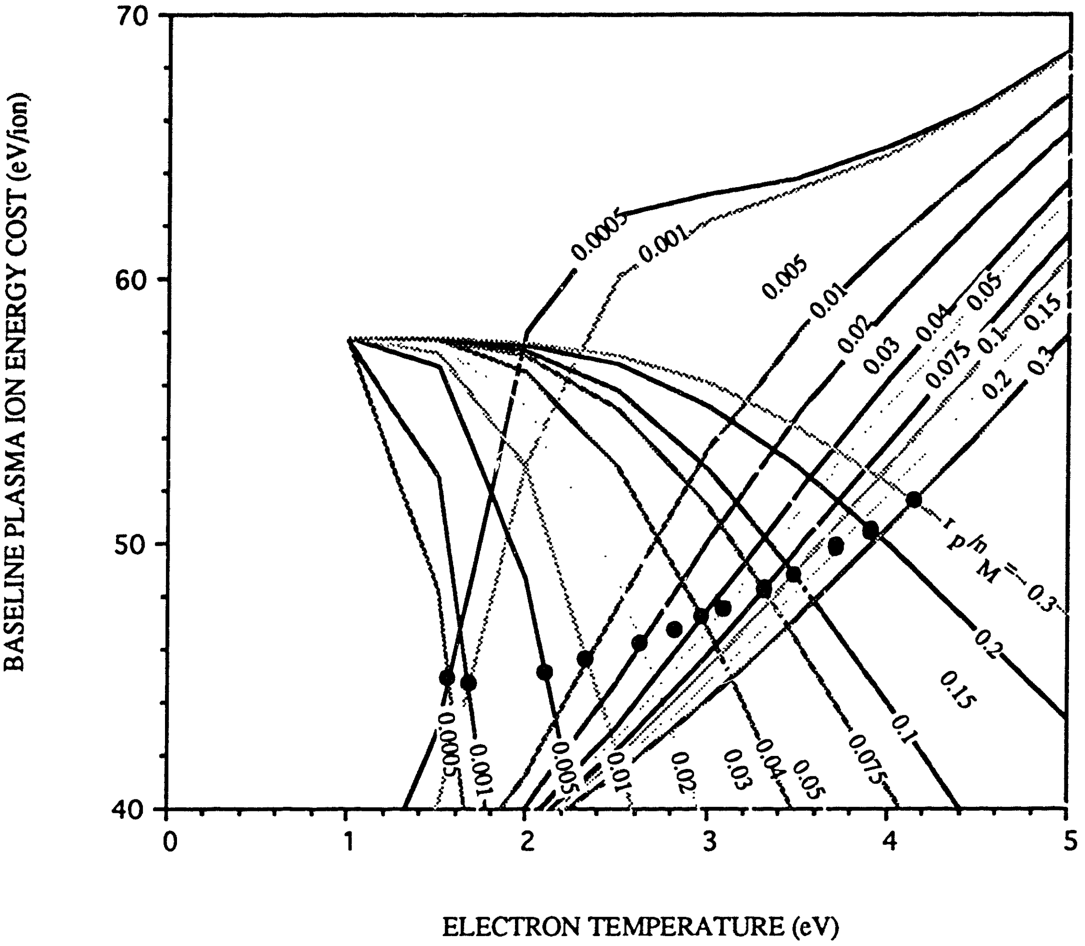

Figure 3.6. Baseline plasma ion energy cost using xenon as the propellant gas and operating at V_D = 30 V.

$$\eta_u = \frac{1}{\left[\frac{0.15\ e\ \varepsilon_p^*\ v_b\ A_g^2\ \phi_o\ \phi_i\ v_o}{J_B\ v_p\ V_D\ f_B V\ \sigma_{t,p}}\right]\left[1 + \frac{n_M}{n_P}\right] + 1} \ . \tag{3.4}$$

The area of the grids A_g was measured to be 0.0537 m^2, and the ion production volume *V* was assumed to be one-half of the discharge chamber volume. The latter assumption is reasonable, since the size of the ion production volume is usually determined by the contour of the 50 G line in typical ring-cusp ion thrusters. In other words, the surface bounded by the 50 G line serves as a virtual anode; any electron that crosses this surface is lost. It is also interesting to note that the failure to close the 50 G line would open a hole through which the plasma can escape from the ion production region. Moreover, since the propellant utilization efficiency only depends linearly on the size of the ion production volume, the precise measurement of this volume is not really needed.

The temperature T_w of the anode walls of the thruster using xenon as the propellant gas was taken to be 450 K, and the thermal velocity v_o of the neutral particles was calculated according to

$$v_o = \sqrt{\frac{8\ k\ T_w}{\pi\ m_{Xe}}} \ , \tag{3.5}$$

where m_{Xe} is the molecular mass of xenon which was taken to be 131 amu and k is the Boltzmann's constant. Finally, the beam current J_B was taken to be 0.405 A from the experiments performed by Reference [18].

Table 3.1 below shows the values of ε_p^*, T_e, n_P/n_M and the corresponding propellant utilization efficiency η_u.

Table 3.1. Propellant utilization efficiency at the equilibrium points calculated for the Hughes 13 cm lab-model thruster using xenon as the propellant gas and running at V_D = 30 V.

n_P/n_M	T_e (eV)	ε_p^* (eV/ion)	η_u
0.0005	1.55	44.75	5.76 %
0.001	1.7	44.75	10.46 %
0.005	2.1	45.25	34.11 %
0.01	2.325	45.75	49.2 %
0.02	2.6	46.5	64.1 %
0.03	2.8	47.0	71.7 %
0.04	2.95	47.5	76.3 %
0.05	3.1	47.75	79.4 %
0.075	3.3	48.5	84.4 %
0.1	3.5	49.25	87.1 %
0.15	3.7	50.0	90.2 %
0.2	3.9	51.4	91.7 %
0.3	4.15	52.0	93.7 %

Section 3.5. Beam Ion Production Cost

Since all the parameters in Eq. (2.10) have been determined, the beam ion production cost ε_B was then calculated as a function of the propellant utilization efficiency. Figure 3.7 on the next page compares the values of the beam ion production cost predicted by Brophy's model and measured experimentally by Reference [18] for the 13 cm lab-model thruster running at 30 V of discharge. The magnitudes of both results agree remarkably well.

The shape of the performance curve for xenon is dominated by the loss of primary electrons to the anode walls. As the propellant utilization efficiency increases, the density of neutral atoms inside the discharge chamber decreases. Therefore, more primary electrons are lost to the anode walls, and the beam ion production cost rises. The same applies to the Maxwellian electrons as shown in Figure 3.6. As the propellant utilization efficiency increases, the neutral density decreases and the Maxwellian electrons do not collide as frequently with the neutral atoms. Since the main mechanism for electron energy loss is through inelastic collisions with the propellant atoms, the electron temperature increases and they are more easily lost to the anode walls. The loss of Maxwellian electrons to the anode walls manifests itself as an increase in the baseline plasma ion energy cost.

Finally, in order to further verify Brophy's model, it was applied again to the 13 cm lab-model thruster, but now operating at higher discharge voltages.

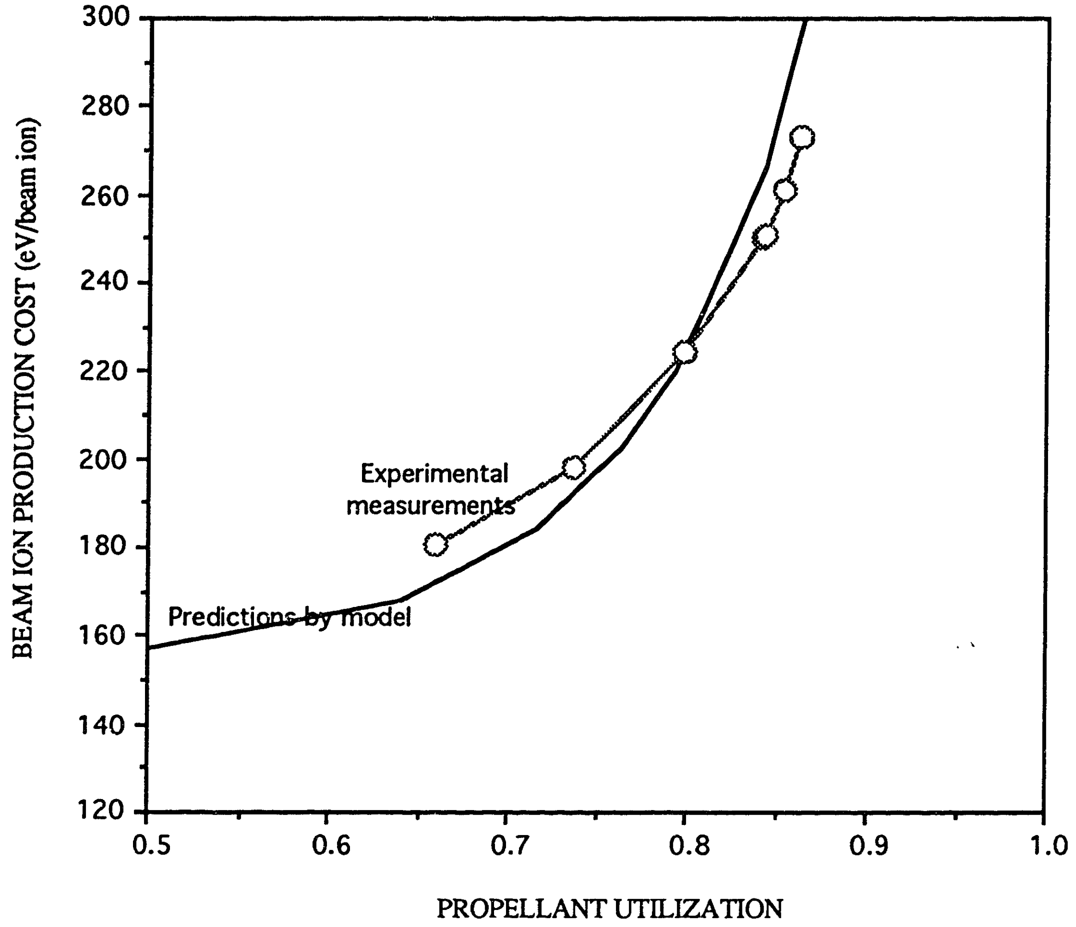

Figure 3.7. Comparison of the values for the beam ion production of the Hughes 13 cm lab-model thruster obtained using Brophy's model and experiments. The propellant gas used was xenon and the discharge voltage was 30 V.

Section 3.6. Higher Discharge Voltages

In order to verify that the model predicted the expected trends for higher discharge voltages as well as to compare the beam ion production cost of xenon and C_{60} at other discharge voltages, the model was applied again to the laboratory-model thruster. Using discharge voltages of 40 V and 50 V, the baseline plasma ion energy was calculated. The results are presented in Figures 3.8 and 3.9 on the next page. They show again that baseline plasma ion energy cost increases as the propellant utilization increases, because more Maxwellian electrons are now being lost to the anode walls. Both figures also show that, in the case of xenon, as one increases the discharge voltage the value of the baseline plasma ion energy cost remains approximately the same at the equilibrium points. However, more power is delivered into the discharge chamber as V_D increases, and this increase in power appears as an increase in the equilibrium electron temperature.

The propellant utilization efficiency was calculated at the equilibrium points using Eq. (3.4). The value of the parameters f_B, f_C, ϕ_i, and ϕ_o used in the case of 30 V were again used at 40 and 50 V. Furthermore, the primary electron utilization factor C_o was recalculated using Eq. (3.1) for the two new discharge voltages. It was found that C_o changed by only 3 %. Finally, the beam ion production cost was computed and is plotted as a function of propellant utilization efficiency in Figure 3.10.

Figure 3.10 shows that in the case of xenon at a constant beam ion production cost, increasing the discharge voltage increases the propellant utilization efficiency for the range of discharge voltages considered. This is expected since for a fixed value of ε_B increasing the discharge voltages increases the power delivered into the discharge chamber by the primary electrons. Hence, the propellant utilization efficiency increases as shown in the experimental measurements of Reference [13].

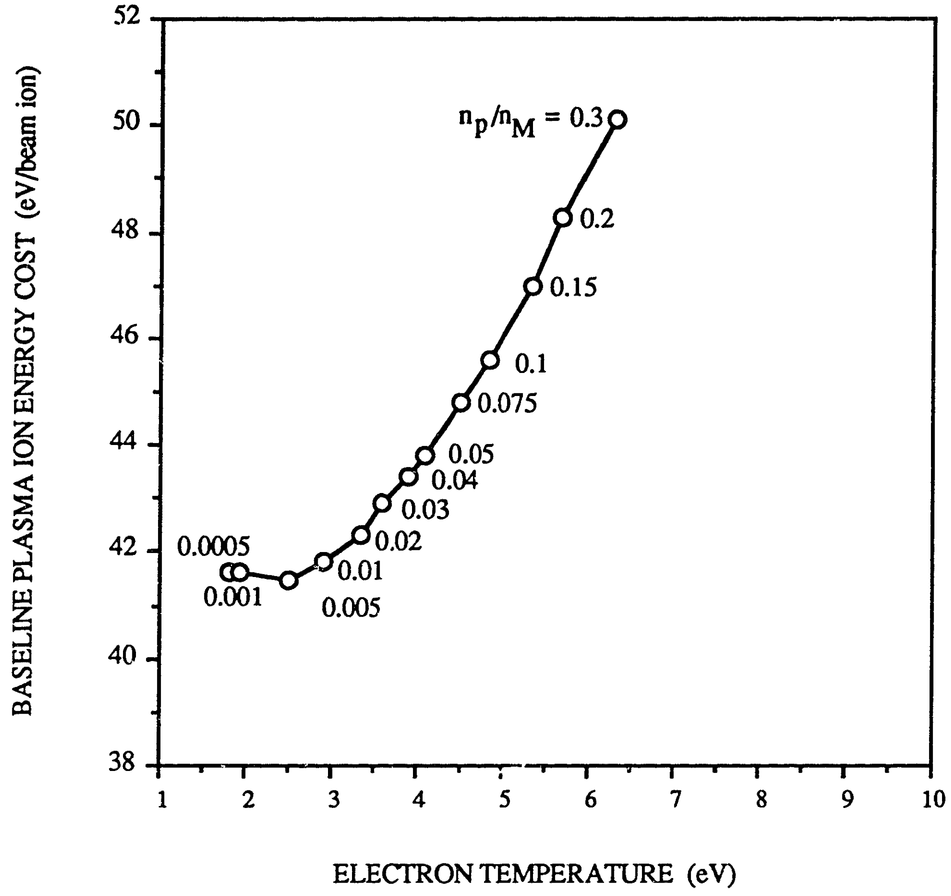

Figure 3.8. Baseline plasma ion energy cost at V_D = 40 V for xenon gas.

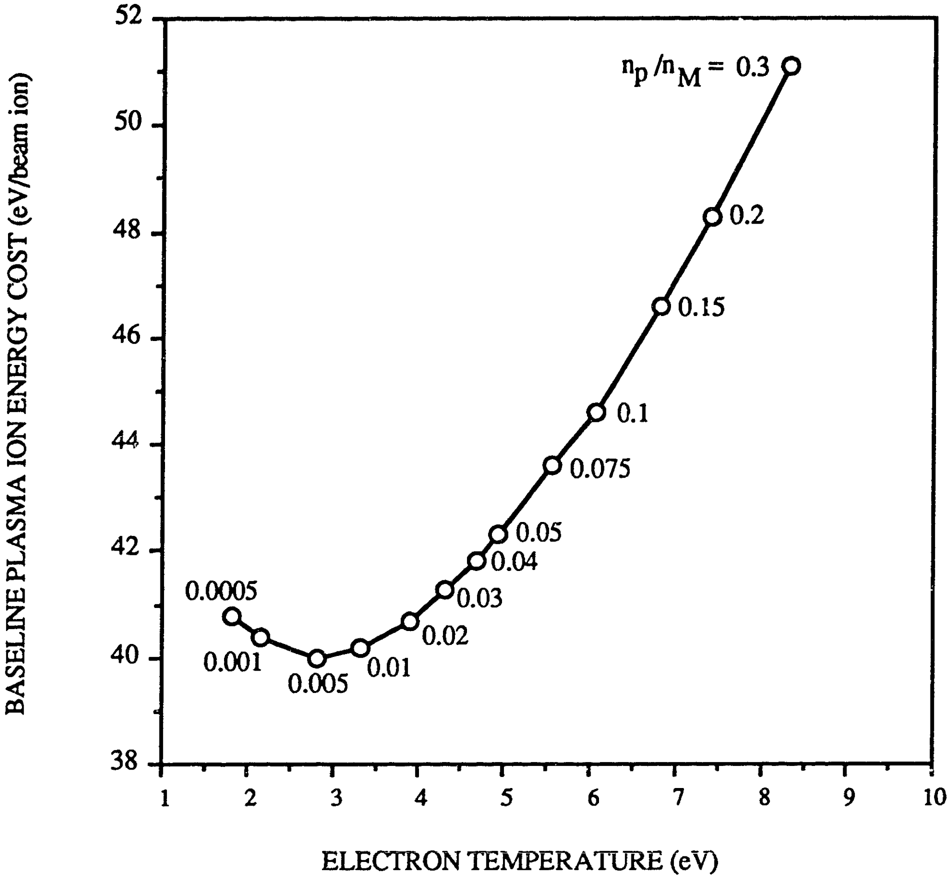

Figure 3.9. Baseline plasma ion energy cost at V_D = 50 V for xenon gas.

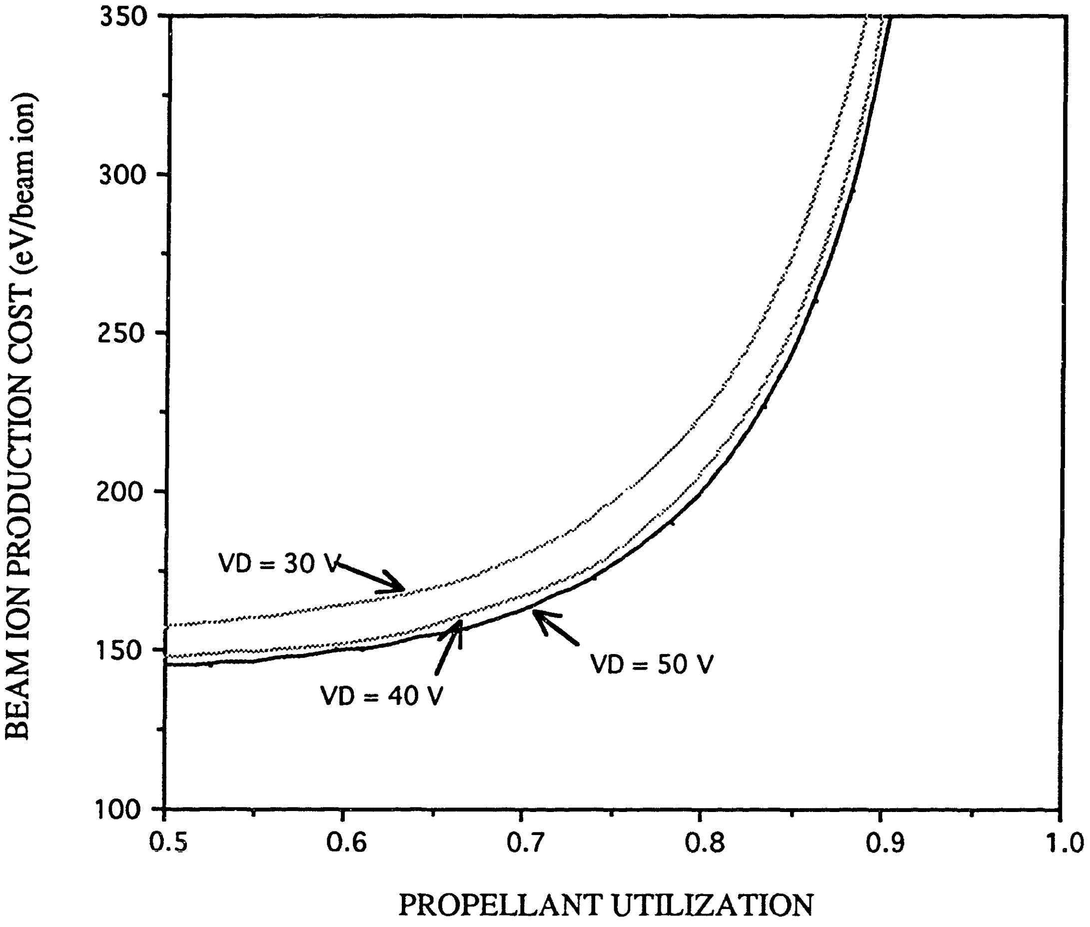

Figure 3.10. Beam ion production cost for the lab-model thruster at different discharge voltages. Propellant gas is xenon.

Chapter 4. Predictions of the Model for Carbon 60

Buckminsterfullerene or carbon 60 is an allotrope of carbon which occurs naturally along with graphite and diamond. Its molecular structure consists of 60 carbon atoms arranged symmetrically in pentagon rings around a spherical shell. Carbon 60 is an attractive candidate for a propellant gas in ion propulsion because it possesses a low ionization threshold energy and a large ionization cross-section for collisions with electrons. However, at the same time it has a low excitation threshold energy and a high excitation cross-section for collisions with electrons, which tend to erode the previous advantages. In order to determine if there are any gains in the performance obtained through the use of carbon 60 as a propellant gas over the currently preferred propellant, xenon, Brophy's model will be applied to the Hughes 13 cm lab-model thruster, now using carbon 60 for the propellant.

The treatment will follow the discussion presented in Chapter 3. The beam ion production cost will be calculated as a function of the propellant utilization efficiency. In order to do so, the terms in the expression for the beam ion production cost, Eq. (2.10), must be determined. The extracted ion fraction f_B and the fraction f_C of ions that are collected by the surfaces at cathode potential will be taken to be 0.3 and 0.1, respectively. Likewise, the transparencies of the ion optics system to ions and neutrals, ϕ_i and ϕ_o, will be taken to be 0.82 and 0.167, respectively. These are the same values that were assumed for the four quantities when xenon was used as the propellant gas, since the dependance of these quantities on the type of propellant is negligible.

However, one must still determine the primary electron utilization factor C_0 and the baseline plasma ion energy cost ε_p^* for carbon 60 in order to compute the beam ion production cost ε_B. Since these two quantities depend on the cross-sections for ionization and excitation of C_{60} molecules by collisions with electrons, one must obtain the values of these cross-sections at different energies. Sai Baba et al. [31] published a paper in which they claimed to have measured the ionization cross-section of C_{60} at an electron energy of 38 eV. The results that his group obtained at other electron energies have not been published yet, but were made available for this research [32]. However, since no one has published measurements of the ionization cross-section at any other energies or the excitation cross-section, the values of these cross-sections will be estimated from the molecular orbitals of carbon 60. The values measured by Reference [32] will be used to check the theoretical calculations.

Section 4.1. Electron Collision Cross-Sections

The ionization and excitation cross-sections of carbon 60 molecules by electrons will be calculated using a theory of inelastic collisions developed by Gryzinski [33-35]. The theory is classical in nature and ignores all aspects of wave mechanics. However, unlike other classical theories such as those advanced by Thompson and Rutherford for Coulomb scattering of electrons by particles at rest, Gryzinski's theory is developed in the laboratory system of coordinates. Furthermore, it takes into account that the electrons inside an atom or molecule are in motion and bound at different energies. From the different energy levels of an atom or molecule, the theory claims to predict the ionization and the excitation cross-section by collisions with particles for the atom or molecule.

Ionization Cross-Section

In order to show the simplicity behind the theory of Gryzinski, consider an atom like hydrogen (H) with single electron at a binding energy of U_i. The ionization cross-section σ for a collision with an electron having an energy E is given by

$$\sigma = \left(\frac{\sigma_o}{U_i^2}\right) g_i(x) , \tag{4.1}$$

where σ_o is 6.54 x 10 $^{-14}$ cm^2, x is the ratio E/U_i, and $g_i(x)$ is given by

$$g_i(x) = \frac{1}{x}\left(\frac{x-1}{x+1}\right)^{3/2} \left[1 + \frac{2}{3}\left(1 - \frac{1}{2x}\right) \ln\left[2.7 + \sqrt{x-1}\,\right]\right] .$$

If there are happened to be two electrons in the atom at the same binding energy, then the previous expression for the ionization cross-section must be multiply by 2 in order to take into account the degeneracy.

Now consider a larger atom like argon with its many electrons at various energy levels with different binding energies. Its electronic configuration is presented in Table 4.1 on the next page. In order to calculate the ionization cross-section of an argon atom, one must first calculate the cross-sections for removing an electron from each of its shells. This partial ionization cross-section is given by Eq. (4.1) where the energy U_i is the binding energy corresponding to that energy level. The cross-section calculated is then multiplied by the corresponding degeneracy of that shell, and the total ionization cross-section is just the sum of the partial ionization cross-sections.

The prediction for the ionization cross-section of argon atoms by collisions with electrons obtained through Gryzinski's theory is presented in Figure 4.1 on the next page. The theory agrees well with experimental measurements shown. Furthermore, notice that most of the contribution to the ionization cross-section comes from the outermost energy level, since its binding energy is the smallest. The contribution of the innermost shell with a binding energy of 3190 eV is almost negligible. Moreover, as one goes deeper into the atom, the contributions of the inner shells occur at larger energies of the incoming electrons, and this keeps the tail end of the cross-section at high energies from approaching zero quickly.

Table 4.1. Atomic structure of argon.

Shell of atom		Degeneracy of shell	Binding Energy of the shell in eV
K	1s	1	3190
L	2s	1	324
L	2p	3	247
M	3s	1	29
M	3p	3	15.7

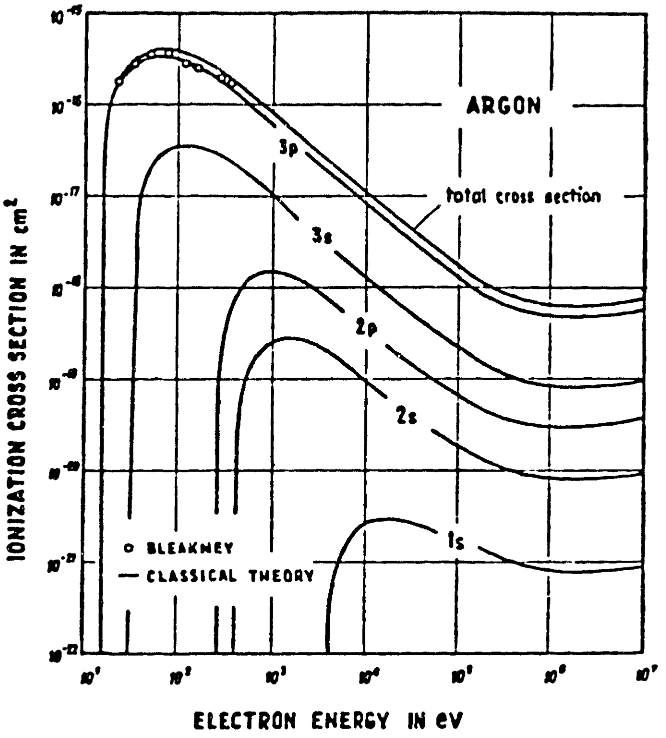

Figure 4.1. Ionization cross-section for argon atoms due to collisions with electrons obtained using Gryzinski's theory [36].

In order to apply the theory developed by Gryzinski to carbon 60, one must first obtain its electronic configuration. The molecular orbitals of carbon 60 computed by Wastberg et al. [37] are presented Table 4.2. Wastberg used the von Barth-Hedin exchange-correlation potential for C_{60} in order to calculate the binding energies of the electrons in each of the molecular orbitals, and his data shows good agreement with the available experimental data. Other authors such as Manousakis [38] and Samuel [39] have predicted similar values. Since the binding energy of the electrons in each of the molecular orbitals is of the same magnitude, the size of the partial cross-sections for each orbital should be about the same. Hence, it would be erroneous to estimate the total ionization cross-section from the binding energy of electrons in the Highest Occupied Molecular Orbital (HOMO).

The total ionization cross-section for carbon 60 was found by summing the partial ionization cross-sections of each molecular orbital. A computer program was written to generate this information. However, after comparing the values of the cross-sections obtained with those values measured by Reference [32], the calculated cross-sections were found to be too large. For example at 45 eV, the calculated cross-section is 5.5×10^{-18} m^2 while the measured one is 6.4×10^{-19} m^2. This discrepancy can be explained on the grounds that the theory advanced by Gryzinski does not take into account wave mechanics which determines the shape and orientation of the molecular orbitals.

Gryzinski's theory works well because the spherical symmetry of an atom allows the electrons to be equally exposed to the incoming electron. However, in a molecule like C_{60} with all its intricate single and double bonds, this may not be the case. In order to take into account that not all the electrons in the C_{60} molecule are equally accessible by an incoming electron, the values calculated for the cross-sections of C_{60} using Gryzinski's theory will all be multiplied by the factor 0.12. This factor is equal to the ratio of the measured ionization cross-section to the cross-section calculated by Gryzinski's theory at 45 eV. This factor was chosen so that the calculated cross-sections would agree better with the measurements, and it is just a "fudge" factor.

A plot comparing the modified Gryzinski cross-sections for ionization and the measured ones is shown in Figure 4.2 on the next page. The agreement is reasonably good.

Table 4.2. Molecular orbitals of C_{60}.

Molecular Orbital	Degeneracy	Binding Energy (eV)
HOMO	5	7.75
HOMO -1	5	8.90
HOMO -2	4	9.00
HOMO -3	5	10.55
HOMO -4	4	10.65
HOMO -5	5	10.95
HOMO -6	3	11.00
HOMO -7	4	12.15
HOMO -8	5	12.30
HOMO -9	3	12.35
HOMO -10	4	12.85
HOMO -11	5	13.25
HOMO -12	3	13.40
HOMO -13	4	13.65
HOMO -14	1	14.00
HOMO -15	3	14.45

Table 4.2. Continued.

Molecular Orbital	Degeneracy	Binding Energy (eV)
HOMO -16	4	15.00
HOMO -17	4	15.25
HOMO -18	4	15.95
HOMO -19	4	17.35
HOMO -20	5	17.75
HOMO -21	3	18.75
HOMO -22	3	19.70
HOMO -23	5	19.95
HOMO -24	4	21.45
HOMO -25	5	21.85
HOMO -26	4	23.20
HOMO -27	3	23.85
HOMO -28	5	24.95
HOMO -29	3	25.90
HOMO -30	1	26.40

As a final note, compare the cross-sections of C_{60} with those of xenon presented in Figure 3.4. The ionization cross-section of C_{60} is about 10 times larger than than of xenon. The threshold ionization energy of C_{60} is just 7.61 eV, while that of xenon is 12.1 eV. These properties indicate that a thruster using C_{60} as the propellant gas would utilize primary electrons more efficiently than when using xenon. However, the overall efficiency of the use of electrons must also take into account the Maxwellians electrons. In order to determine this efficiency, the excitation cross-section by collisions with electrons must be computed.

Excitation Cross-Section

The theory of inelastic collisions developed by Gryzinski will be again used to calculate the excitation cross-sections of carbon 60. As shown in Reference [34], this theory works well for the excitation of atoms. However, when dealing with molecules, discrepancies will arise.

The total excitation cross-section is the sum of the excitation cross-section of each of the allowable transitions. This partial cross-section for a transition from a molecular orbital p to an orbital q is given by

$$\sigma_{ex} = Q\left(\frac{U_p^i}{U_{p,q}}, \frac{E}{U_{p,q}}\right) - Q\left(\frac{U_p^i}{U_{p,q+1}}, \frac{E}{U_{p,q+1}}\right),$$

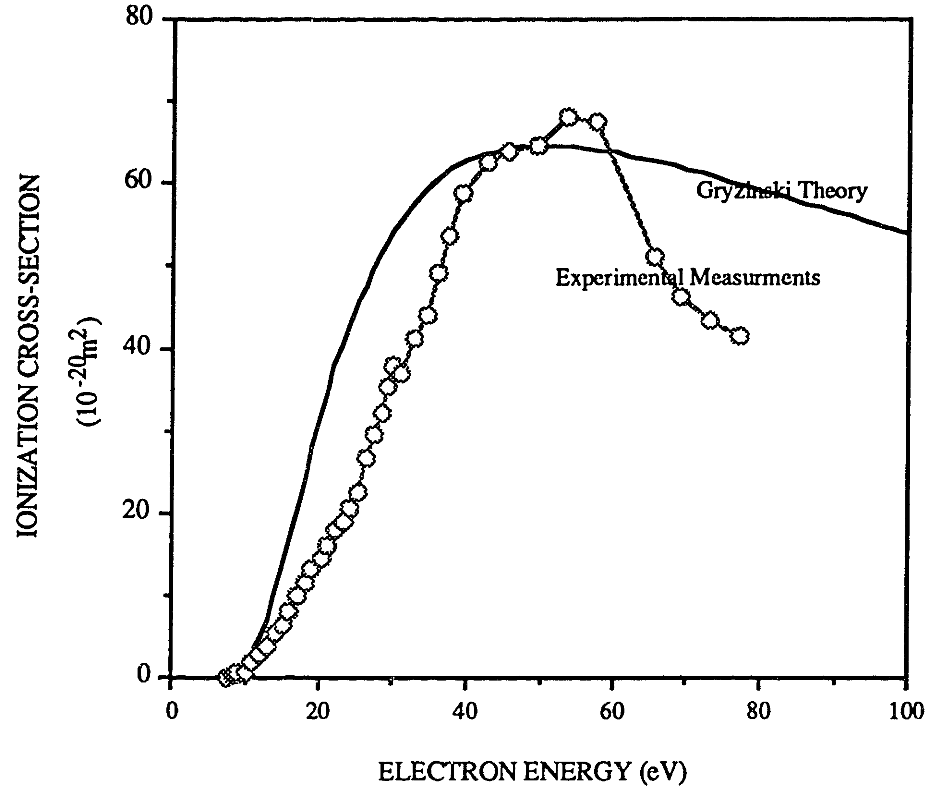

Figure 4.2. Comparison of the ionization cross-section calculated by Gryzinski's theory and measured experimentally for carbon 60. Note that experimental results are yet to be published.

where $U_{p,q}$ is the energy difference between level p and q, $U_{p,q+1}$ is the energy difference between level p and the next allowable level from q, and U_p^i is the binding energy of level p. In turn, the functions Q are given as

$$Q\left(\frac{U_p^i}{U_{p,q}}, \frac{E}{U_{p,q}}\right) = \frac{\sigma_o}{U_{p,q}^2}\, g_Q \, .$$

By defining ε to be $E/U_{p,q}$ and $A = U_p/U_{p,q}$, the term g_Q becomes

$$g_Q = \left(\frac{\varepsilon}{A+\varepsilon}\right)^{3/2}\left[\frac{1}{\varepsilon} + \frac{1}{3}\,\frac{A}{\varepsilon^2}\,(2\varepsilon - 1)\ln\left[e + \sqrt{\frac{\varepsilon - 1}{A}}\,\right]\right]\left[1 - \frac{1}{\varepsilon}\right]^{\frac{2A+1}{A+1}} ,$$

where e refers to 2.7187.

The allowable transitions of C_{60} are shown in Table 4.3 with the corresponding transition energies. These transitions were obtained from Reference [37] by applying the even to odd or odd to even transition rule. A program was again written to calculate the cross-section for each of these allowable transitions. The cross-section computed for each transition was then multiplied by a factor that took into account the degeneracy of the starting state p and the number of available states that the electron could go into.

For example, consider the transition from HOMO to LUMO + 3. The degeneracy of HOMO is 5, while the degeneracy of LUMO + 3 is 5. Suppose now that an incoming electron had an energy larger than 5.9 eV, but lower than 7.75 eV. It could excite an electron in the HOMO orbital into either the LUMO+1, LUMO+3, or LUMO+5 orbitals. In order to take into account that an electron in the HOMO orbital could go into all these many orbitals, not just LUMO + 3, the cross-section calculated using the transition energies required to go between HOMO and LUMO + 3 was multiplied by the factor

$$\begin{pmatrix}\text{Degeneracy}\\ \text{of}\\ \text{HOMO}\end{pmatrix}\frac{\begin{pmatrix}\text{Degeneracy}\\ \text{of}\\ \text{LUMO +3}\end{pmatrix}}{\begin{pmatrix}\text{Degeneracy}\\ \text{of}\\ \text{LUMO +1}\end{pmatrix}+\begin{pmatrix}\text{Degeneracy}\\ \text{of}\\ \text{LUMO +3}\end{pmatrix}+\begin{pmatrix}\text{Degeneracy}\\ \text{of}\\ \text{LUMO +5}\end{pmatrix}}\,.$$

Similarly, if the incoming electron had an energy larger than 3.95 eV but less than 5.9 eV, the cross-section calculated for the transition from HOMO to LUMO +3 would be multiplied by

$$\begin{pmatrix}\text{Degeneracy}\\ \text{of}\\ \text{HOMO}\end{pmatrix}\frac{\begin{pmatrix}\text{Degeneracy}\\ \text{of}\\ \text{LUMO +3}\end{pmatrix}}{\begin{pmatrix}\text{Degeneracy}\\ \text{of}\\ \text{LUMO +1}\end{pmatrix}+\begin{pmatrix}\text{Degeneracy}\\ \text{of}\\ \text{LUMO +3}\end{pmatrix}}\,.$$

Factors like these were used to take into account the many different states an electron could be excited into during a transition. The cross-sections calculated for each allowable transition were then summed up to find the total excitation cross-section as a function of the incoming electron energy. Finally, the values obtained for the total excitation cross-section were multiplied by the factor 0.12 that was used to force the ionization cross-sections calculated using Gryzinski's theory agree with the experimental measurements.

Table 4.3. Allowable transitions of C_{60}.

Molecular Orbital p	Binding Energy (eV) U_p^i	Allowable transitions to other orbitals q	Energy difference (eV) $U_{p,q}$
HOMO	7.75	LUMO + 1 LUMO + 3 LUMO + 5	2.85 3.95 5.9
HOMO -1	8.90	LUMO LUMO + 2 LUMO + 4	2.90 4.95 6.45
HOMO -2	9.00	LUMO LUMO + 2 LUMO + 4	3.00 5.05 6.55
HOMO -3	10.55	LUMO + 1 LUMO + 3 LUMO + 5	5.60 6.70 8.65
HOMO -4	10.65	LUMO + 1 LUMO + 3 LUMO + 5	5.70 6.80 8.75
HOMO -5	10.95	LUMO LUMO + 2 LUMO + 4	4.95 7.00 8.5
HOMO -6	11.00	LUMO + 1 LUMO + 3 LUMO + 5	6.10 7.20 9.15

Table 4.3. Continued.

Molecular Orbital p	Binding Energy (eV) U_p^i	Allowable transitions to other orbitals q	Energy differenc (eV) $U_{p,q}$
HOMO -7	12.15	LUMO + 1 LUMO + 3 LUMO + 5	7.15 8.25 10.2
HOMO -8	12.30	LUMO LUMO + 2 LUMO + 4	6.3 8.35 9.85
HOMO -9	12.35	LUMO LUMO + 2 LUMO + 4	6.45 8.5 10.0
HOMO -10	12.85	LUMO LUMO + 2 LUMO + 4	6.9 8.5 10.45
HOMO -11	13.25	LUMO LUMO + 2 LUMO + 4	7.25 9.3 10.8
HOMO -12	13.40	LUMO + 1 LUMO + 3 LUMO + 5	8.5 9.6 11.55
HOMO -13	13.65	LUMO + 1 LUMO + 3 LUMO + 5	8.7 9.8 11.75

Table 4.3. Continued.

Molecular Orbital p	Binding Energy (eV) U_p^i	Allowable transitions to other orbitals q	Energy difference (eV) $U_{p,q}$
HOMO -14	14.0	LUMO LUMO + 2 LUMO + 4	8.05 10.1 11.6
HOMO -15	14.45	LUMO + 1 LUMO + 3 LUMO + 5	9.5 10.6 12.15
HOMO -16	15.0	LUMO + 1 LUMO + 3 LUMO + 5	10.05 11.15 13.1
HOMO -17	15.25	LUMO + 1 LUMO + 3 LUMO + 5	10.3 11.4 13.35
HOMO -18	15.95	LUMO LUMO + 2 LUMO + 4	9.95 12.0 13.5
HOMO -19	17.35	LUMO LUMO + 2 LUMO + 4	11.3 13.35 14.85
HOMO -20	17.75	LUMO LUMO + 2 LUMO + 4	11.75 13.8 15.3

Table 4.3. Continued.

Molecular Orbital p	Binding Energy (eV) U_p^i	Allowable transitions to other orbitals q	Energy difference (eV) $U_{p,q}$
HOMO -21	18.75	LUMO + 1	13.8
		LUMO + 3	14.9
		LUMO + 5	16.85
HOMO -22	19.7	LUMO + 1	14.7
		LUMO + 3	15.8
		LUMO + 5	17.75
HOMO -23	19.95	LUMO + 1	14.95
		LUMO + 3	16.05
		LUMO + 5	18.0
HOMO -24	21.45	LUMO	15.4
		LUMO + 2	17.45
		LUMO + 4	18.95
HOMO -25	21.85	LUMO	15.8
		LUMO + 2	17.85
		LUMO + 4	19.35
HOMO -26	23.2	LUMO + 1	18.2
		LUMO + 3	19.3
		LUMO + 5	21.25
HOMO -27	23.85	LUMO + 1	18.85
		LUMO + 3	19.95
		LUMO + 5	21.9

Table 4.3. Continued.

Molecular Orbital p	Binding Energy (eV) U_p^i	Allowable transitions to other orbitals q	Energy difference (eV) $U_{p,q}$
HOMO -28	24.95	LUMO LUMO + 2 LUMO + 4	18.9 20.95 22.45
HOMO -29	25.9	LUMO + 1 LUMO + 3 LUMO + 5	20.9 22.0 23.95
HOMO -30	26.4	LUMO LUMO + 2 LUMO + 4	20.35 22.4 23.9

The final results for the excitation collision cross-section are plotted in Figure 4.3 on the next page. Comparing these values with those measured for xenon shows that the excitation cross-section of C_{60} is about an order of magnitude higher than that of xenon.

The excitation cross-sections presented in Figure 4.3 should be taken as a rough estimate, of the same order of magnitude, for the actual excitation collision cross-section of carbon 60 molecules with electrons. These excitation cross-sections have not been measured yet, mainly because much of the scientific research has been devoted to bombarding C_{60} molecules with heavy particles in order to investigate the strength of its spherical structure and its fracture mechanisms. As compared with neutrons, electrons are relatively benign and would pose no threat of breaking the C_{60} spherical shell. Nevertheless, scientists at the Jet Propulsion Laboratory hope to measure these cross-sections in the near future.

However, in order to apply Brophy's model and obtain reliable results, estimates of the cross-sections that are within an order of magnitude should be sufficient. Furthermore, since the excitation cross-sections have not been measured, the ionization and excitation cross-sections calculated using Gryzinski's theory will be used in the application of Brophy's model.

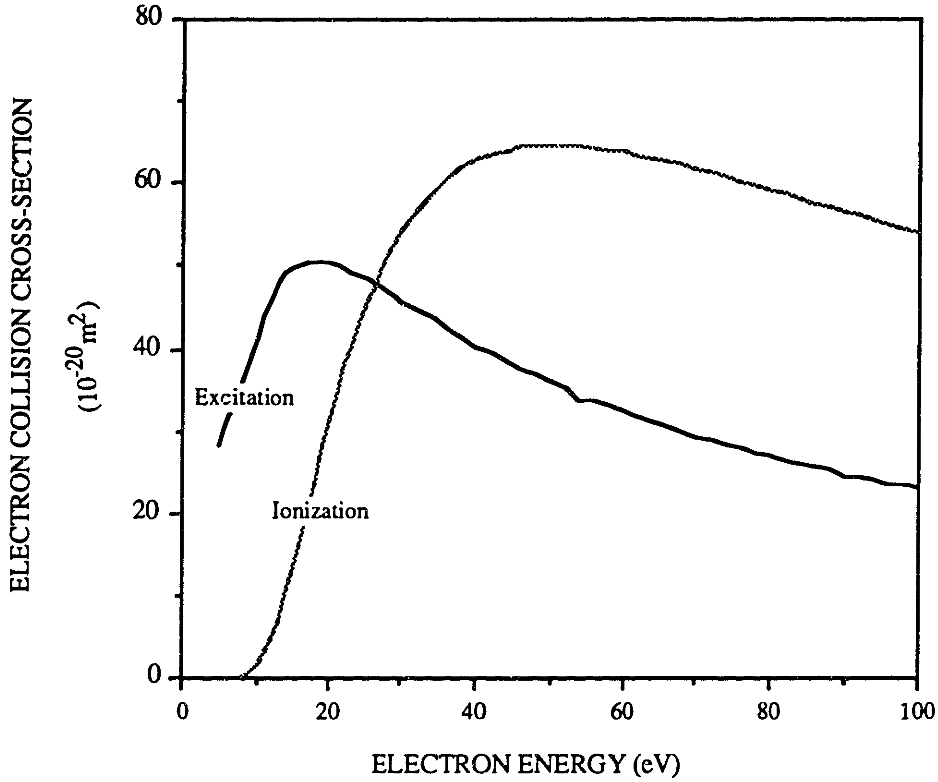

Figure 4.3. Excitation cross-section of C_{60} molecules by collisions with electrons.

Section 4.2. Primary Electron Utilization Factor

Equation (3.1) in the beginning Chapter 3 showed the dependance of the primary electron utilization factor C_o on the type of the propellant gas and the design of the discharge chamber of a thruster. Since the primary electron containment length l_e does not depend on the type of propellant used, it is a constant of the thruster and has the same value whether the thruster uses carbon 60 or xenon. One can obtain the primary electron utilization factor of the 13 cm lab-model thruster using C_{60} through the ratio

$$\frac{C_{o,\,C60}}{C_{o,\,Xe}} = \left(\frac{\sigma_{t,p,C60}}{\sigma_{t,p,Xe}}\right) \left(\frac{v_{o,\,Xe}}{v_{o,\,C60}}\right) \left(\frac{l_{e,C60}}{l_{e,Xe}}\right),$$

where $\sigma_{t,p,C60}$ and $\sigma_{t,p,Xe}$ refer to the total inelastic collision cross-section of carbon 60 and xenon at the primary electron energy and $v_{o,Xe}$ and $v_{o,C60}$ are thermal velocity of xenon atoms and C_{60} molecules, respectively. Using the constancy of l_e and Eq. (3.5) for the thermal velocity of neutrals, the ratio is transformed into

$$\frac{C_{o,\,C60}}{C_{o,\,Xe}} = \left(\frac{\sigma_{t,pri,C60}}{\sigma_{t,pri,Xe}}\right) \sqrt{\frac{T_{w,\,Xe}}{T_{w,\,C60}}} \sqrt{\frac{m_{C60}}{m_{Xe}}} \;.$$

At a discharge voltage of 30 V where a typical ion thruster using xenon normally operates, the ratio of the total inelastic collision cross-section of C_{60} to that xenon was calculated to be 13.5. Realizing that the mass of a C_{60} molecule is 5.34 times that of a xenon molecule and assuming the anode walls of a thruster running on C_{60} are at the same temperature, approximately 450 K, as that of a xenon thruster, the ratio of the primary electron utilization factors becomes

$$\left[\frac{C_{o,\,C_{60}}}{C_{o,\,Xe}}\right]_{T_{w,C_{60}} = T_{w,Xe}} = 31.66\,.$$

Finally, taking into account that C_o was computed to be 12.32 for xenon in Chapter 3, the primary electron utilization factor for C_{60} at 30 V is 390.1 A^{-1}.

However, the temperature of the anode walls in a carbon 60 thruster would most likely be larger than 450 K in order keep the C_{60} molecules from striking and condensing on the walls of the anode. Since carbon 60 is an insulator, coatings of C_{60} on any part on the inside of the discharge chamber may lead to electrical open circuits, in which a critical part of the thruster may be isolated from the rest of the body. Since the typical pressures inside the discharge chamber are on the order of 10^{-3} Torr, the anode walls should be kept at the sublimation temperature corresponding to this pressure. This temperature was measured by Abrefah et al. [39] to be 825 K. Taking into account this higher wall temperature, the ratio of the primary electron utilization factors becomes

$$\frac{C_{o,\,C_{60}}}{C_{o,\,Xe}} = 22.16\,.$$

This ratio is much higher than the ratio of 6 predicted by Reference [9]. Using the higher anode wall temperature, the primary electron utilization factor for the Hughes 13 cm lab-model thruster running on C_{60} at a discharge voltage of 30 V was calculated to be 273.1 A^{-1}.

The higher wall temperature of the anode reduces the efficiency with which the thruster uses the primary electrons, since the C_{60} neutral molecules are more mobile through the chamber. However, since the magnitude of C_0 is already very large, compared to typical values which are usually less than 10 A^{-1}, the decrease is not very significant. Moreover, the large primary electron utilization factor of C_{60} allows a thruster to run at higher propellant utilization efficiencies while maintaining efficient use of the primaries which keeps beam ion production cost low. The relationship between the beam ion production cost and the propellant utilization efficiency drawn in Figure 3.10 becomes more like a 90 degree angle, and the knee of the curve moves to higher propellant utilization efficiencies.

In order to quantify the reduction in the beam ion production cost by the use of C_{60} as a propellant gas, one must calculate the baseline plasma ion energy cost.

Section 4.3. Baseline Plasma Ion Energy Cost

The baseline plasma ion energy cost was calculated in the same manner as was done for xenon in Chapter 3. The cross-sections used were those obtained using Gryzinski's theory in order to remain consistent, since the excitation cross-sections have not been measured yet. The rate coefficients for ionization and excitation by Maxwellian electrons were then computed for these cross-sections. The results are plotted on the page 96.

Notice that the rate coefficients for carbon 60 for both excitation and ionization are larger than those of xenon.

In order to compare the baseline plasma ion energy cost of a thruster using carbon 60 to that of a thruster using xenon, the discharge voltage V_D was taken to be 30 V, since this was the same voltage at which the experimental measurements for the 13 cm lab-model thruster using xenon were performed. Moreover, V_C was taken to be 5 V as was done for xenon in Chapter 3.

Figure 4.5 shows the results obtained for the baseline plasma ion energy cost. Comparing these results with those obtained for xenon in Figure 3.6, one notices that the baseline plasma ion energy cost for both gases has the same order of magnitude. For both gases as the electron temperature rises, the ratio of the density of primary electrons to secondary electrons also rises. This is expected regardless of the type of the propellant gas. However, in the range of electron temperatures considered as the electron temperature increases, the baseline plasma ion energy cost for xenon rises, while that of C_{60} decreases. This phenomenon shows two mechanisms which influence the baseline plasma ion energy cost:

In the case of C_{60} at very low electron temperatures, the baseline plasma ion energy cost is at its maximum value given by

$$\varepsilon_p^* = V_D \frac{\sigma_{t,p}}{\sigma_{+,p}} ,$$

where the cross-sections are evaluated at the primary electron energy. Even though the

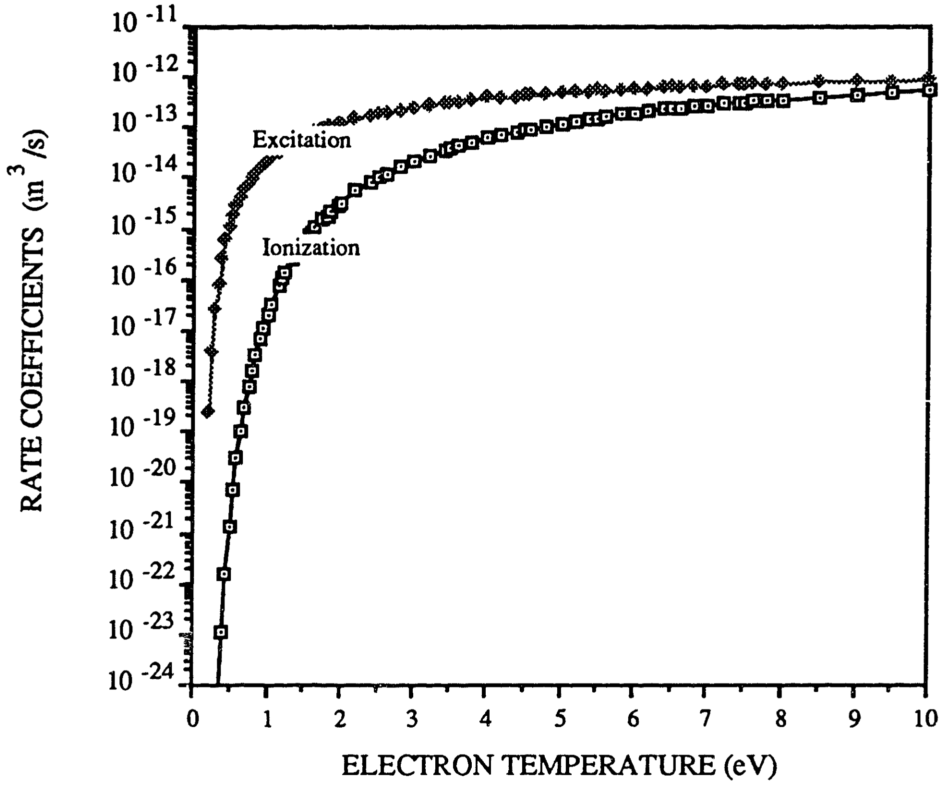

Figure 4.4. Rate coefficients for the ionization and excitation of C_{60} molecules by collisions with Maxwellian electrons.

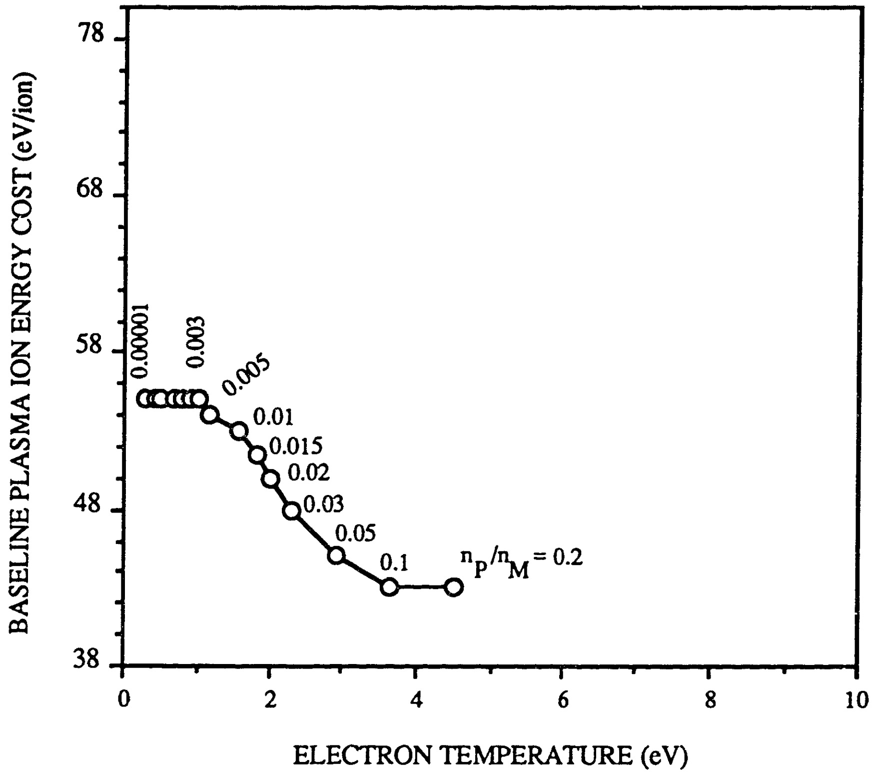

Figure 4.5. Baseline plasma ion energy cost for carbon 60 at V_D = 30 V.

density of primary electrons is small relative to the density of Maxwellian electrons, the electron temperature is small enough that all of the ionization is being performed by the primary electrons. One can verify this proposition analytically by inserting the value of the baseline plasma ion energy cost into Eq. (2.5). As the electron temperature increases, it makes two contributions to baseline plasma ion energy cost: (1) more Maxwellian electrons are now being lost to the anode walls, and (2) the ionization rate by Maxwellians increases. At the low temperatures (less than 2.5 eV) obtained for C_{60}, the increase in the ionization rate coefficient dominates over the loss of Maxwellian electrons to the anode walls. This in turn causes the ion production rate by Maxwellian electrons to increase, and the baseline plasma ion energy cost therefore decreases. Notice the shape of the ionizaton rate coefficient curve in Figure 4.4.

In the case of xenon the electron temperature is already larger than in the case of C_{60}. Therefore, as the electron temperature increases, the increase in the ionization rate is not large enough to offset the loss of Maxwellian electrons to the walls of the anode. Hence, the baseline plasma ion energy cost increases. This hypothesis also explains why the baseline plasma ion energy cost curve for C_{60} starts to slope upwards after about 4 eV, when the loss of Maxwellian electrons becomes dominant.

Furthermore, the electron temperature is lower in the case of C_{60} than in the case of xenon, because the ionization and excitation thresholds are lower in C_{60} as shown in Table 1.1. Any electron with an energy above these thresholds is likely to lose its energy quickly through inelastic collisions, and this will happen in the case of carbon 60 to a greater extent.

Section 4.4. Beam Ion Production Cost

In order to calculate the beam ion production cost for the 13 cm lab-model thruster, one must first compute the propellant utilization efficiency. This calculation was performed by evaluating Eq. (3.4) at each of the equilibrium points in Figure 4.5. The beam current was taken to be 0.5 A. The anode wall temperatures was first taken to be 450 K and then 825 K. The table on the next page presents the propellant utilization efficiency using both wall temperatures.

The higher wall temperature for a C_{60} thruster leads to a lower propellant utilization efficiency at each of the equilibrium points, since the neutral molecules are more mobile about the chamber. Moreover, notice that the difference in the efficiencies decreases as η_u increases. At higher propellant utilization efficiencies the number of neutrals around the discharge chamber decreases, and hence their temperature does not have a large influence on the value of the propellant utilization efficiency.

Finally, compare the results for η_u obtained using C_{60} and those obtained for xenon in Table 3.1. The propellant utilization efficiency is always greater for C_{60} than for xenon, because of the larger electron collision cross-sections.

Eq. (2.10) was then used to compute the beam ion production cost at each of the propellant utilization efficiencies. The wall temperature of the anode was assumed to be 825 K; the corresponding primary electron utilization factor was taken to be 270 A^{-1}; and the propellant utilization efficiency was taken from the last column in Table 4.4. Figure 4.6 plots the beam ion production cost versus η_u for the Hughes 13 cm lab-model thruster either using xenon or C_{60} as the propellant gas at a discharge voltage $V_D = 30$ V.

Table 4.4. Equilibrium points and η_u for 13 cm lab-model thruster using C_{60} as the propellant gas at V_D = 30 V.

n_P/n_M	T_e (eV)	ε_P^* (eV/ion)	η_u T_w = 450 K	η_u T_w = 825 K
0.00001	0.3	55	19 %	14 %
0.00005	0.45	55	49 %	40 %
0.0001	0.5	55	64.5 %	55.9 %
0.0002	0.52	55	78.1 %	71.3 %
0.0005	0.7	55	88.5 %	84.3 %
0.001	0.8	55	93.5 %	90.93 %
0.002	0.9	55	96.4 %	94.971 %
0.003	1.0	55	97.47 %	96.409 %
0.005	1.15	54	98.38 %	97.696 %
0.01	1.55	53	99.068 %	98.668 %
0.015	1.8	52	99.3449 %	99.0619 %
0.02	2.0	50	99.493 %	99.2748 %
0.03	2.3	48	99.648 %	99.4963 %
0.05	2.9	45	99.872 %	99.675115 %
0.1	3.65	43	99.872 %	99.8173 %
0.2	4.5	43	99.9228 %	99.889272 %

In the case of carbon 60 the beam ion production cost remains relatively flat until very high propellant utilization efficiencies, while in the case of xenon ε_B starts rising fairly early. Since the shape of the performance curves is primarily determined by the loss of electrons to the anode walls, Figure 4.6 proves that buckminsterfullerene is more efficient in utilizing primary electrons. Furthermore, the flat portion of the beam ion production cost curve for carbon 60 is given by

$$\varepsilon_B = V_D \frac{\sigma_{t,p}}{\sigma_{+,p}} \frac{1}{f_B} + \frac{f_C}{f_B} V_D ,$$

since the plasma ion energy cost ε_p is constant along this portion and equal to the maximum baseline plasma ion energy cost.

However, as the propellant utilization efficiency increases beyond 96 %, the beam ion production cost increases. Two mechanisms are at work here. The baseline plasma ion energy cost ε_p^* decreases as shown in Table 4.4 and Figure 4.5 because the Maxwellian electrons start contributing to the ionization process. Nevertheless, this decrease in ε_p^* is not enough to make up for the increase in cost due to the fact that more primary electrons are now being lost to the anode walls. Therefore, the beam ion production cost increases. If there was a way that the decrease in ε_p^* would dominate over the loss of primary electrons to the anode walls, then the beam ion production cost would decrease, and hence the performance curve would show a dip.

Comparing the beam ion production cost of xenon and C_{60}, there is a clear advantage in operating a thruster with C_{60} at propellant utilization efficiencies greater 70 %. In order to find the optimal operating point of the C_{60} performance curve in Figure 4.6,

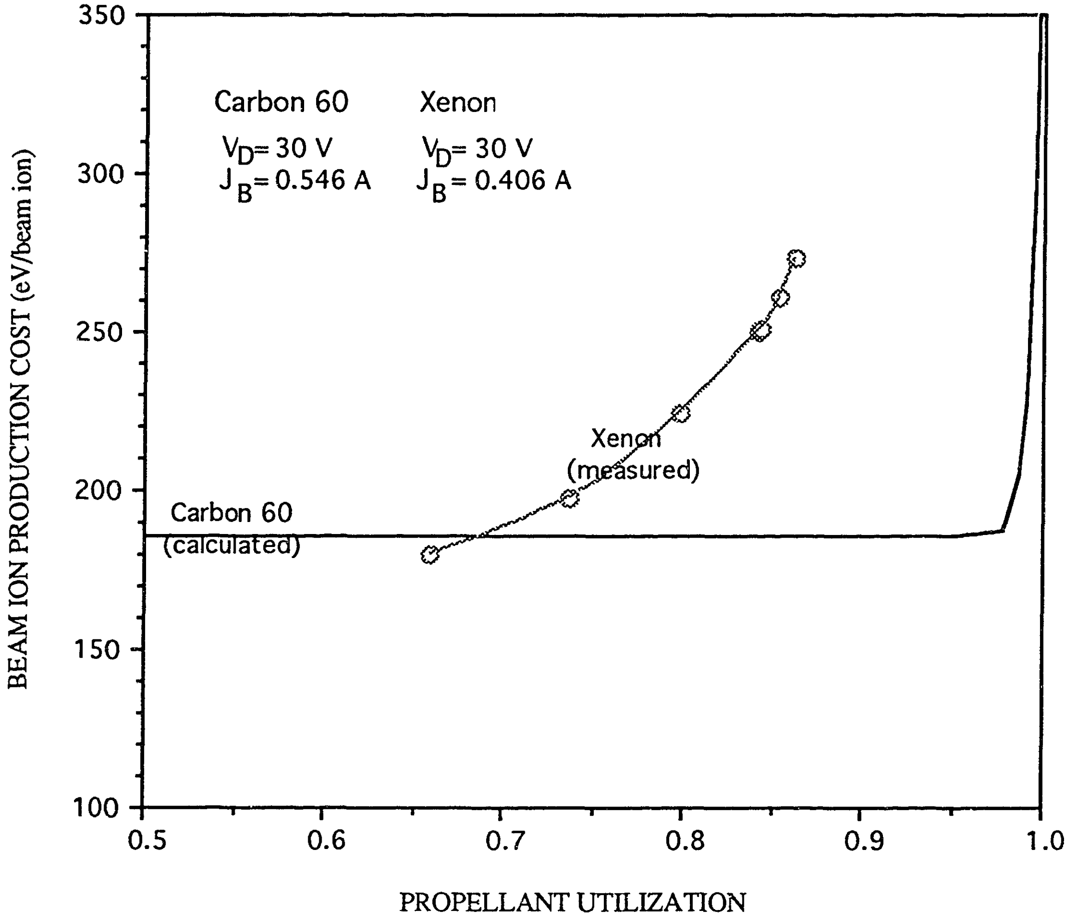

Figure 4.6. Beam ion production cost for the Hughes 13 cm lab-model thruster using xenon or carbon 60 for the propellant gas. V_D = 30 V.

one must consider the production of doubly-charged ions.

Section 4.5. Formation of Doubly-Charged Ions

Doubly-charged ions are typically formed at very high propellant utilizations. They are harmful and should be avoided because of mainly two reasons. First, the ion optics system of a thruster is designed to extract and focus only singly-charged ions. Doubly-charged ions that make their way to the grids are not properly focused and their trajectories may strike the accelerator grid. Many ions at high energies striking the accelerator grid eventually erode it, decreasing the lifetime of the ion thruster. Second, it costs energy to remove an electron from a singly-charged C_{60} ion. This energy could be better used to ionize more neutral C_{60} molecules.

The production rate of doubly-charged ions is given by

$$J_P^{++} = (n_o n_M Q_o^{++} + n_o n_P P_o^{++} + n_i n_M Q_+^{++} + n_i n_P P_+^{++})\, 2e\,,$$

where Q_0^{++} and P_0^{++} are the rate coefficients for direct double ionization of a neutral C_{60} molecule, Q_+^{++} and P_+^{++} are the rate coefficients for second ionization of a C_{60} ion, and n_i is the density of C_{60} ions inside the discharge chamber. In order to determine the production rate of doubly-charged ions, the cross-sections for removing an electron from a positive C_{60} ion were calculated using the Gryzinski theory, and the molecular orbitals of the C_{60} ion were obtained from Reference [37]. However, there was no theory to calculate the direct double ionization of a C_{60} molecule, and hence the first two terms in the ion production rate were neglected. Dividing the previous equation by the production rate of singly-charged ions,

$$J_P^+ = (n_o n_M Q_o^+ + n_o n_P P_o^+)e,$$

one obtains the ratio

$$\frac{J_P^{++}}{J_P^+} = \frac{\frac{2n_i}{n_o}\left(Q_+^{++} + \frac{n_P}{n_M}P_+^{++}\right)}{Q_o^+ + \frac{n_P}{n_M}P_o^+},$$

The density n_i of ions can be approximated using Eq. (2.8) by assuming that the beam consists only of singly-charged ions. Furthermore, the neutral density n_o is given by Eq. (2.7). Entering these two expressions into the equation for the ratio of doubly to singly-charged ions, one obtains an expression for the ratio of doubly to singly-charged ion production rates:

$$\frac{J_P^{++}}{J_P^+} = 0.83 \left(\frac{v_o}{v_b}\right)\left(\frac{\phi_o}{\phi_i}\right)\left(\frac{\frac{2n_+}{n_o}\left(Q_+^{++} + \frac{n_P}{n_M}P_+^{++}\right)}{Q_o^+ + \frac{n_P}{n_M}P_o^+}\right)\left[\frac{\eta_u}{1 - \eta_u}\right].$$

This ratio was then tabulated along the performance curve presented in Figure 4.6 for buckminsterfullerene. The results are presented on the next page.

Table 4.5. Ratio of doubly to singly-charged ion production rates as a function of the propellant utilization efficiency.

η_u	$\frac{J_P^{++}}{J_P^{+}}$
40 %	0.00836
84 %	0.043
90 %	**0.076**
95 %	0.1338
98 %	0.2711
99 %	0.407
99.5 %	0.845

The ratio of the ion production rates of doubly to singly-charged ions increases as the propellant utilization efficiency increases. The operating point with η_u equal to 90 % appears to be the optimum since operating at a greater propellant utilization efficiency increases the number of doubly-charged ions tremendously. The larger number of doubly-charged ions leads to a higher rate of sputtering of the accelerator grid. Moreover, a beam ion production cost higher than the one presented in Figure 4.6 results because power that would go into ionizing C_{60} molecules is now lost by removing another electron from a C_{60} ion.

Section 4.6. Higher Discharge Voltages

In order to further compare the performance of the 13 cm lab-model thruster obtained using either C_{60} or xenon as the propellant gas, Brophy's model will be applied again at discharge voltages $V_D = 40$ V and $V_D = 50$ V. The anode wall temperature was assumed to be 825 K, and at these new discharge voltages the primary electron utilization factor was calculated to be 285 and 281, respectively. Figures 4.7 and 4.8 plot the dependance of the baseline plasma ion energy cost on electron temperature and ratio of the primary to Maxwellian electrons.

The shape of the curves is similar to the ones obtained for $V_D = 30$ V. However, the variation in the baseline plasma ion energy cost is larger. At low electron temperatures which correspond to low ratios of primary to Maxwellian electrons, the baseline plasma ion energy cost flattens out onto a maximum. This maximum increases as the discharge voltage increases. Along this portion of the curve, all of the ionization is being carried out by the primary electrons. The Maxwellian electrons play no role. They are just strolling around the chamber possibly exciting the C_{60} molecules but not ionizing any of them.

Increasing the discharge voltage from 30 to 40 to 50 V increases the power that is being delivered into the chamber. The ionization cross-section increases and the excitation cross-section decreases, but not by much. However, the power that is transferred into the Maxwellian electron group when the primaries undergo inelastic collisions is still lost through excitations of the C_{60} molecules by Maxwellian electrons. More of this power is lost as the discharge voltage increases since the ionization cross-section does not rise by much relative to the excitation cross-section. The outcome is that more power is applied to the thruster to obtain the same ion production rate. Therefore, the cost of producing an ion in the chamber increases, and this increase is reflected in the rise of the baseline plasma ion energy cost at low electron temperatures.

As the electron temperature increases, Maxwellians begin to take part in the ionization process. The baseline plasma ion energy cost decreases to reflect the higher ion production rate. Notice that for a given ε_p^* and n_P/n_M the electron temperature increases as the discharge voltage increases. This occurs because as V_D increases the primary electrons collide with higher energies against the C_{60} molecules. More energy is transferred into the Maxwellian electron group, and the primary electrons that are degraded to secondaries have a wider distribution in energy. This reflected in a higher electron temperature.

The beam ion production cost at these higher voltages is plotted in Figure 4.9. In the case of C_{60}, the shape of the performance curve is dominated by the baseline plasma ion energy cost at propellant utilization efficiencies less than 95 %. In other words, buckminsterfullerene is so efficient in utilizing the primary electrons that their loss to the anode walls does not play a role until very high propellant utilization efficiencies. Therefore, the changes in the beam ion production cost for η_u less than 95 % are the changes in ε_p^* discussed in the previous paragraphs.

As the discharge voltage increases the beam ion production cost increases because more power is being applied to the thruster for the same ion production rate. The Maxwellian electrons are not contributing to the ionization process. As the propellant utilization efficiency increases, the neutral density decreases and the electron temperature increases. A dip in the performance curve then occurs shown in Figure 4.9 for the cases of $V_D = 40$ and 50 V when the Maxwellian electrons start ionizing the C_{60} molecules. As η_u increases further, the loss of primary electrons to the anode walls becomes dominant and hence the beam ion production cost increases. The results for $V_D = 40$ and 50 V are merely

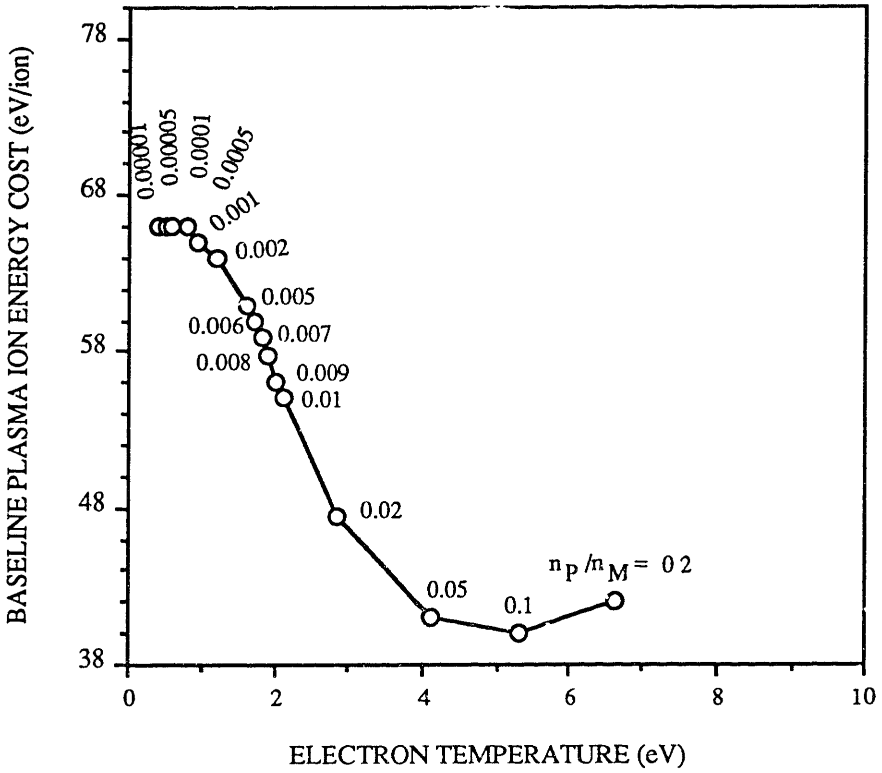

Figure 4.7. Baseline plasma ion energy cost for C_{60} at V_D = 40 V.

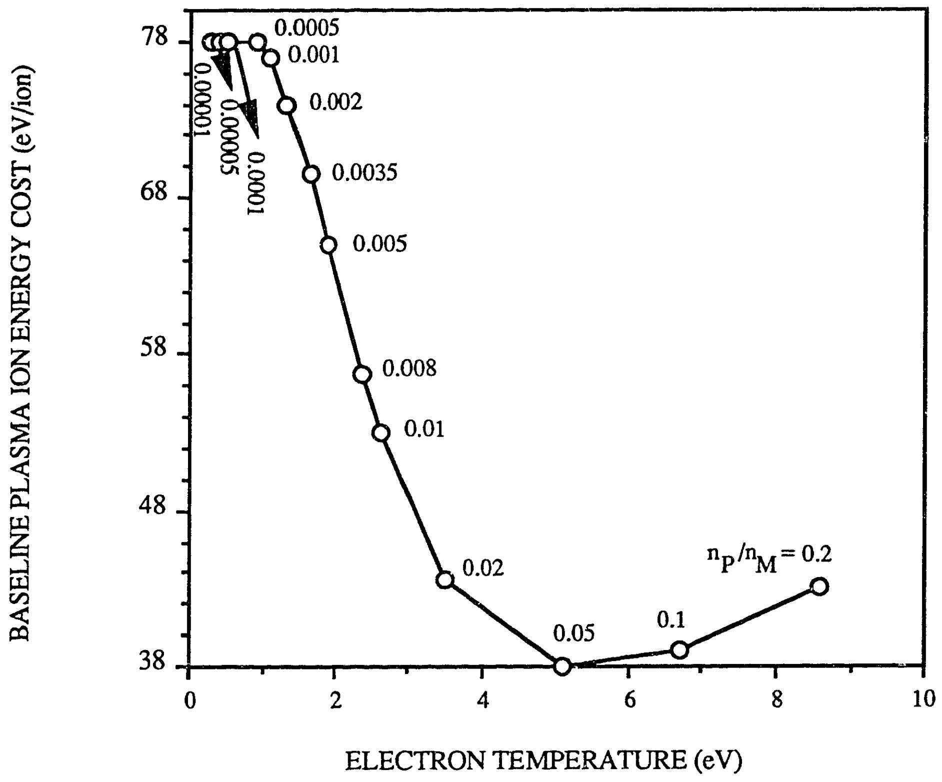

Figure 4.8. Baseline plasma ion energy cost for C_{60} at $V_D = 50$ V.

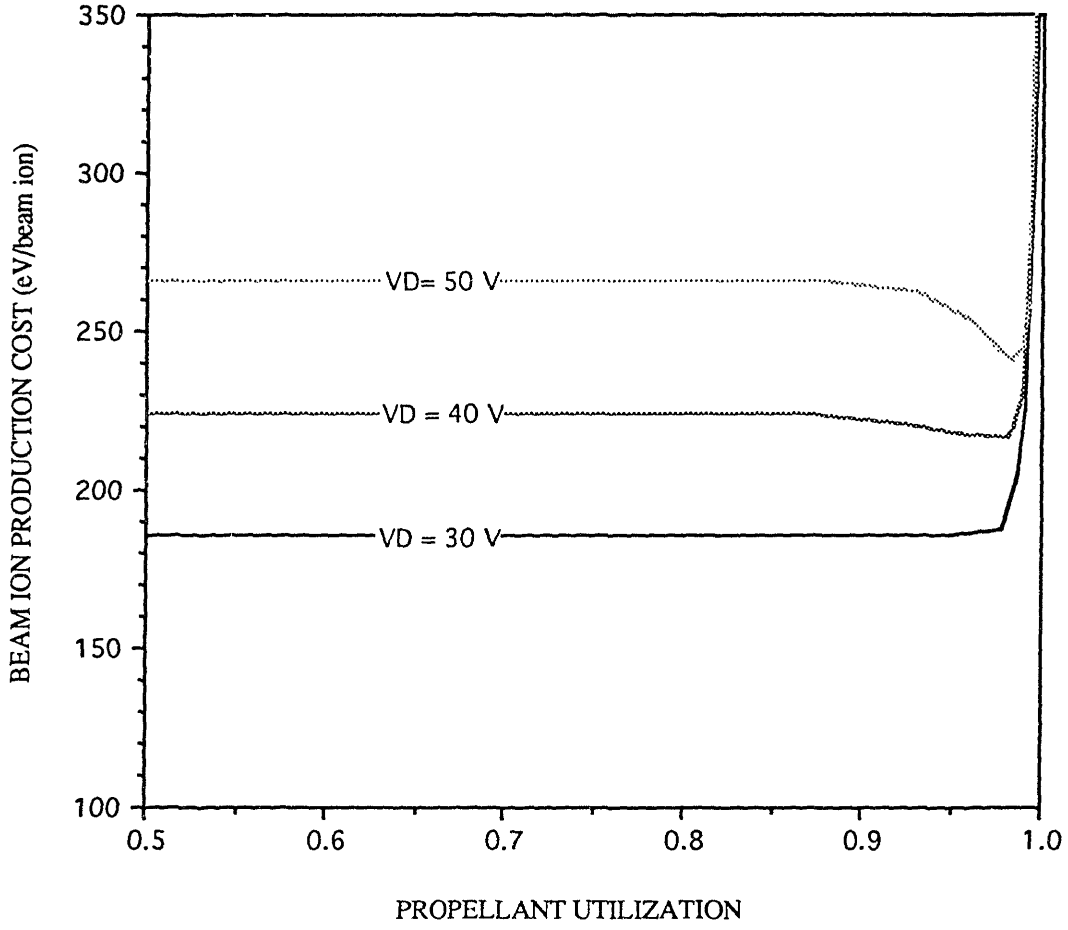

Figure 4.9. Beam ion production cost for the Hughes 13 cm lab-model thruster at different discharge voltages. The propellant used is C_{60}.

academic, because no one would run a thruster at those discharge voltages when a lower beam ion production cost would be obtained at lower discharge voltages.

Section 4.7. Optimum Discharge Voltage

Figure 4.9 suggests that there should be an optimum discharge voltage at which the value of beam ion production cost along the flat portion of the performance curve is the smallest. Along this flat portion, the baseline plasma ion energy cost is at its maximum given by

$$\varepsilon_p^* = V_D \frac{\sigma_{t,p}}{\sigma_{+,p}} . \tag{4.2}$$

Table 4.6 on the next page shows the maximum baseline plasma ion energy cost at different discharge voltages. The results show that at a discharge voltage of 22 V the maximum baseline ion energy cost is at a minimum. Hence, the beam ion production cost is also at a minimum given by 177 eV/beam ion. Furthermore, one must still keep in mind that the cross-sections used were calculated using Gryzinski's theory. In real life, ε_B will be minimized when the Eq. (4.2) is at a minimum, and this minimum will be close, but necessarily exactly equal to a discharge voltage of 22 V. Table 4.7 presents the optimal operating parameters at this discharge voltage.

Table 4.6. Potential optimum discharge voltage for a C_{60} ion thruster.

V_D (V)	$V_D \frac{\sigma_{t,p}}{\sigma_{+,p}}$ (eV/ion)
30	55.226
27	52.77
25	51.65
24	51.26
22	**51.03**
20	51.99
18	55.44
17	58.82

Table 4.7. Predicted parameters of a potential optimal operating point for a C_{60} ion thruster.

V_D	22 V
ε_B	177 eV/beam ion
η_u	90 %
T_e	0.85 eV
$\frac{n_P}{n_M}$	0.0025
$\frac{J_P^{++}}{J_P^{+}}$	0.057

Section 4.8. Formation of Negative C_{60} Ions

Since carbon 60 molecules may attract electrons more easily than other gases used in ion propulsion as stipulated in Reference [9], a calculation will be performed to check if the formation of negative C_{60} ions inside the discharge chamber is negligible. This worry emanates from two facts. The energy for electron attachment of C_{60} molecules is 2.75 eV . Moreover, the previous calculations showed the Maxwellian electrons in a typical C_{60} ion thruster have an electron temperature lower than 1 eV. Since these electrons are not ionizing the propellant gas, the question becomes then what is happening to these electrons. Assuming that the negative ions are effectively trapped, and therefore their rates of creation and destruction must be equal, the density of negative C_{60} ions will be calculated as a function of the Maxwellian electron temperature using statistical mechanics to determine the relevant equilibrium constant.

The formation of negative C_{60} ions is governed by the reaction,

$$C_{60} + e^- \rightarrow C_{60}^- .$$

Using partition functions, one can relate the density of C_{60} molecules, negative C_{60} ions, and electrons which from now on will be labeled with brackets as in $[e^-]$. The previous equation for the formation of negative C_{60} ions indicates that densities are related by

$$\frac{[C_{60}^-]}{[C_{60}]\,[e^-]} = \frac{\zeta_{C_{60}^-}}{\zeta_{C_{60}}\zeta_e} , \qquad (4.3)$$

where the ζ's refer to the partition function of C_{60}, negative C_{60} ions, and electrons.

The densities of electrons and C_{60} neutral molecules in the chamber can be calculated as a function of the Maxwellian electron temperature using the formulation developed in Chapter 2. Assuming that the plasma inside the discharge chamber obeys quasi-neutrality, the density $[e^-]$ of electrons can be written as

$$\Gamma_i = [e^-]\ v_b\ \phi_i = \frac{J}{e},$$

where J is the current density and can be approximated for a given accelerating voltage using the Child-Langmuir Law. The Bohm velocity is known as a function of electron temperature. Furthermore, the density of C_{60} neutral molecules in the chamber can be obtained using the definition the propellant utilization efficiency. In other words,

$$\frac{\Gamma_i}{\Gamma_i + \Gamma_n} = \frac{[e^-]\ v_b\ \phi_i}{[e^-]\ v_b\ \phi_i + [C_{60}]\ \frac{v_o}{4}\ \phi_o} = \eta_u,$$

where Γ_n refers to the flux of C_{60} molecules inside the chamber. Assuming a propellant utilization efficiency of 80 % for simplicity, the density of C_{60} neutral molecules can then be calculated as a function of electron temperature. However, in order to calculate the density of negative C_{60} ions inside the chamber, the partition functions must be computed.

If the electron energy is taken to be zero for an electron at rest, the partition function for electrons is simply given by

$$\zeta_e = \frac{2}{h^3} (2 \pi \ m \ k \ T_e)^{3/2} \ ,$$

where h refers to Planck's constant, 6.6 x 10^{-34} J·sec, and m to the mass of the electron, 9.1 x10^{-31} kg. The partition functions for C_{60} neutral molecules and C_{60} negative ions are more difficult to calculate. In general the partition function for a neutral C_{60} molecule can be written as

$$\zeta_{C_{60}} = \sum_{s}^{all} \exp(-\beta \ \varepsilon_s) \ ,$$

where s refers to all quantum states of the molecule, ε_s is the energy of the state s, and β is the Boltzmann's factor. The different quantum states of the molecule can be divided into translational, electronic, rotational, and vibrational states. Hence, the partition function for the molecule is the product of the partition function of each of the different states. In other words,

$$\zeta_{C_{60}} = \zeta_{Translation} \ * \ \zeta_{electronic} \ * \ \zeta_{rotational} \ * \zeta_{vibrational} \ .$$

A negative C_{60} ion is produced by the capture of an electron by a neutral C_{60} molecule. The addition of the electron should not alter the mass or molecular structure of the molecule by much. Therefore, the translational, rotational, and vibrational states of a neutral C_{60} molecule and a negative C_{60} ion should be approximately the same. Hence, the ratio of the partition functions of a neutral C_{60} molecule to the negative ion is given by

$$\frac{\zeta_{C_{60}^-}}{\zeta_{C_{60}}} = \frac{\zeta_{\mathrm{electronic},\ C_{60}^-}}{\zeta_{\mathrm{electronic},\ C_{60}}} \exp\left(\frac{\varepsilon_{\mathrm{attach}}}{k\,T_e}\right) = \frac{\sum\limits_{s,\ C_{60}^-} \omega(\varepsilon_s) \exp(-\beta\,\varepsilon_s)}{\sum\limits_{s,\ C_{60}} \omega(\varepsilon_s) \exp(-\beta\,\varepsilon_s)} \exp\left(\frac{\varepsilon_{\mathrm{attach}}}{k\,T_e}\right),$$

where the sum is over all the electronic states s, and $\omega(\varepsilon_s)$ refers to the degeneracy of the electronic state corresponding to the energy ε_s, and $\varepsilon_{\mathrm{attach}}$ refers to the energy of attachment.

Using the electronic states of C_{60} and the negative ion computed by Reference [38], Eq (4.3) was then solved for the density of negative C_{60} ions inside the discharge chamber as a function of the temperature of Maxwellian electrons. In the range of temperatures where a C_{60} ion thruster would normally operate, about 1 eV, the density of negative C_{60} ions is eight to nine order of magnitudes lower than the density of C_{60} neutral molecules as shown Table 4.8 on the next page. Therefore, one should be able to neglect the formation of negative C_{60} ions.

Table 4.8. Estimates of the ratio of the density of negative C_{60} ions to neutral molecules inside the discharge chamber.

T_e (eV)	$\frac{[C_{60}^-]}{[C_{60}]}$
1.0	4.15×10^{-9}
0.86	8.12×10^{-9}
0.7	2.40×10^{-8}
0.5	2.01×10^{-7}
0.3	1.73×10^{-5}
0.2	2.63×10^{-3}

Chapter 5. Conclusions and Recommendations

Using the values of the beam ion production cost calculated in Chapter 4 for buckminsterfullerene, the performance of a C_{60} ion thruster will be compared with those of competing electric propulsion devices. Afterwards, hurdles will be identified that must be overcome in order to build and operate a C_{60} ion thruster.

Section 5.1. Performance Comparisons

There are several technologies that compete against a C_{60} ion thruster. One is the Russian Stationary Plasma Thruster (SPT) that generated considerable interest when it was first introduced into the United States in 1991 [41]. It has already flown on various Soviet spaceflights and the Loral Corporation has exclusive rights to develop and market the SPT within the USA.

Since SPT is feared as a serious challenge toward ion propulsion, the thrust and I_{sp} of the SPT-100 will be used to find the beam voltage and beam current required of a C_{60} ion thruster to produce the same performance. The thrust is determined by

$$T = \gamma \frac{J_B}{e} v_B ,$$

where v_B is the velocity of ions in the beam and γ was taken to be 0.97. By relating the beam ion velocity to the beam voltage and setting the thrust T equal to 80 mN, which is the thrust level produced by the SPT-100 during efficient operation [42], one obtains a relation between the beam current and beam voltage:

$$T = 3.878\ \gamma\ J_B \sqrt{V_B} = 80. \tag{5.1}$$

On the other hand, the specific impulse is given by

$$I_{sp} = \frac{\gamma \eta_u}{g_o} \sqrt{\frac{2\,e\,V_B}{m_{C_{60}}}}\ .$$

Setting this expression equal to the I_{sp} of the SPT-100 thruster, 1600 sec obtained from Reference [42], one obtains a relation between the beam voltage and the propellant utilization efficiency:

$$I_{sp} = 52.75\,\gamma\,\eta_u \sqrt{V_B} = 1600\ . \tag{5.2}$$

Knowing the propellant utilization efficiency, one can solve for V_B and J_B. In Section 4.5 it was shown that that up to a propellant utilization efficiency of 90 %, the production of doubly-charged ions was not important. Taking η_u to be 90 % yields a value of V_B equal to 1207 V and J_B equal to 0.613 A.

In Chapter 4 we found an optimum discharge voltage, namely $V_D = 22$ V, for operating a C_{60} ion thruster. This operating point led to a beam ion production cost of 177 eV/beam ion. Operating at this discharge voltage and at 90 % utilization, the total power used by the C_{60} ion thruster becomes

$$P_T = P_{misc} + (177)(0.613) + (1207)(0.613) ,$$

where P_{misc} takes into account miscellaneous power used by the thruster. As a first approximation, P_{misc} will be taken to be equal to the miscellaneous power used by typical Hughes 13 cm thrusters when operating on xenon gas, namely 33.5 W. Therefore, the total power used by the C_{60} thruster is equal to 882 W.

Table 5.1 compares the performance of the Russian SPT-100 thruster, the Hughes 13 cm lab-model thruster using C_{60}, a Hughes 13 cm xenon ion thruster, and a typical low power arcjet presented in Reference [3]. An ion thruster running on on C_{60} offers considerably better performance than a Russian SPT thruster. It can provide the same thrust and specific impulse at a much lower amount of input power. Similarly, a C_{60} ion thruster offers a higher thrust to power ratio than a similar ion thruster operating on xenon gas. Furthermore, it also offers a higher specific impulse than a low power arcjet.

The previous results combined with those of Chapter 4 show that carbon 60 offers substantial performance gains for ion thrusters. In order to make these gains a reality some hurdles must be overcome in order to actually operate a C_{60} ion thruster.

Table 5.1. Performance comparison of a C_{60} ion thruster and competing electric propulsion thrusters.

Peformance Parameter	SPT-100	**13 cm Ion Thruster**		Typical Low Power Arcjet
		C_{60}	Xe	
Thrust (mN)	80	**80**	18	198
Total Power (W)	1350	**882**	439	1260
Thrust/Power (mN/kW)	59.3	**90**	40.6	157
Specific Impulse (sec)	1600	**1600**	2585	460

Section 5.2. Experimental Work

After predicting the performance curves of the Hughes 13 cm lab-model thruster, this thruster was operated at the Hughes Research Laboratories with a mixture of buckminsterfullerene and xenon. The intent was to measure the beam ion production cost, but two problems occurred which prevented the measurements. These were how to feed the C_{60} material into the discharge chamber and how to the keep the inside of the discharge chamber hot enough to prevent C_{60} molecules from condensing on it.

In order to feed buckminsterfullerene into the chamber, a 1/4 inch tube was used. The C_{60} material was pressed into one inch pellets and inserted inside the tube. A heater from a hollow cathode was then wrapped around the outside of the evaporator tube. Furthermore, the tube was calibrated by placing it inside a vacuum chamber and applying a current for 10 minutes. Then, the C_{60} was collected with an Erlenmayer flask as it evaporated from the tube. The collected C_{60} was then weighed and the average flow rate was computed. The process was repeated at different currents ranging from 0.5 A to 4.0 A. The average flow rates obtained were less than 1 mg/sec. Furthermore, not all of the C_{60} inside the tube evaporated. Some of it actually converted to graphite.

Using this evaporator tube, buckminsterfullerene was fed into the discharge chamber. However, the flow rate could not be controlled because it could not be measured. A better way of feeding C_{60} and controlling the flow rate into the discharge chamber must be developed.

Another problem encountered was the fact that C_{60} can deposit on the inside walls of the discharge chamber as was mentioned in Section 4.2. The temperature of the anode walls must then be increased to 825 K. However, in a ring-cusp thruster like the Hughes 13 cm lab-model thruster, the permanent magnets are placed along the inside of the discharge chamber, and these magnets start to lose their magnetization above 550 K. Therefore, three rings of radiation shields were wrapped around the inside wall of the chamber. The idea was that the discharge plasma would heat the outer shield above 825 K, while the inner one would remained cool enough to pose no threat to the magnets.

After operating the ion thruster with buckminsterfullerene and xenon, the grids were removed to visually inspect the thruster. It was found that on some runs C_{60} had actually alloyed with the surface of the outer radiation shield. On other runs, there were flakes of black soot all over the inside of the chamber. No thermocouple was connected to the outer shield so its temperature was never measured. These findings suggest that a C_{60} ion thruster could benefit from using electromagnets rather than permanent magnets. Finally, it was observed that on all runs C_{60} had coated the screen grid along a surface marked by the area of the beam.

Section 5.3. Recommendations

The work that remains to be performed now is twofold. First, the excitation cross-section of C_{60} molecules by collisons with electrons needs to be measured. These measurements will allow a more accurate prediction of the performance of a C_{60} ion thruster than the one presented here. Second, an ion thruster must be run with carbon 60 as the propellant to obtain performance curves experimentally. In order to do so, the problems presented in Section 5.2 must be overcome, as well as others that may come up. Until an ion thruster is operated on buckminsterfullerene at steady state, one will never know all of the performance benefits obtained from the use of C_{60}.

References

1. Fearn, D. G., “Ion Propulsion: Science Fiction Becoming Science Fact,” *Spaceflight*, Vol. 34, October 1992.

2. Jahn, R. G., **Physics of Electric Propulsion**, McGraw-Hill Book Company, New York, 1968.

3. Beattie, J. R. and Penn, J. P., “Electric Propulsion - A National Capability,” AIAA-89-2490, July 1989, p. 5.

4. Hill, Phillip G. and Peterson, Carl R., **Mechanics and Thermodynamics of Propulsion**, Addision-Wesley Publishing Company, Reading, 1970.

5. Beattie, J. R., Matossian, J. N., and Robson, R. R., “Status of Xenon Ion Propulsion Technology,” AIAA-87-1003, May 1987, p. 2.

6. Prof. Manuel Martinez-Sanchez’s notes for 16.532, as well as private communications.

7. Private communication with Dr. John R. Beattie, Hughes Research Laboratories.

8. Kroto, H. W., Heath, J. R., O’Brien, S. C., Curl, R. F., and Smalley, R. E., "C_{60}: Buckminsterfullerene," *Nature* 1985, 318. p. 162-163.

9. Leifer, S. and Saunders, W., “Electrostatic Propulsion Using C60 Molecules,” IPEC-91-154, October 1991.

10. Diederich, Francois and Whetten, Robert, “Beyond C_{60}: The Higher Fullerenes,” *Acc. Chem. Res.*, 1992, 5, p. 119-126.

11. Matossian, J. N. and Beattie, J. R., “Model for Computing Volume-Averaged Plasma Properties in Electron-Bombardment Ion Thrusters,” *Journal of Propulsion and Power,* Vol. 5, No. 2, 1989.

12. Longhurst, G. R. and Wilbur, P. J., "Plasma Properties and Performance Prediction for Mercury Ion Thrusters," AIAA-79-2054, November 1979.

13. Brophy, J. R., "Ion Thruster Performance Model," NASA CR-174810.

14. Matossian and Beattie, p. 189.

15. Brophy, John R. and Wilbur, Paul J., "An Experimental Investigation of Cusped Magnetic Field Discharge Chambers," *AIAA Journal*, Vol. 24, No. 1, January 1986.

16. Divergilio, W. F., Goede, H., and Fosnight, V., "High Frequency Plasma Generators for Ion Thrusters," NASA CR-167957.

17. Brophy, J. R. and Wilbur, P. J., "Simple Performance Model for Ring and Line Cusp Ion Thrusters," *AIAA Journal*, Vol. 23, No. 11.

18. Beattie, J. R., Robson, R. R., and Williams, J. D., "18-mN Xenon Ion Propulsion Subsystem," IPEC-91-010, October 1991.

19. Beattie, Robson, and Williams, p. 4.

20. Beattie, Robson, and Williams, p. 6.

21. Arakawa, Y. and Ishihara, K., " A Numerical Code for Cusped Ion Thrusters," IPEC-91-118, October 1991.

22. Arakawa, Y. and Yamada, T., "Monte Carlo Simulation of Primary Electron Motions in Cusped Discharge Chambers," AIAA-90-2654, Orlando 1990.

23. Arakawa and Yamada, p. 3.

24. Vaugh, J. A. and Wilbur, P. J., "Ring Cusp/Hollow Cathode Discharge Chamber Performance Studies," Proceedings of the 20th International Electric Propulsion Conference, 1988.

25. Private communication with Dr. J. N. Matossian, Hughes Research Labortatories.

26. Private communication with Dr. John R. Beattie.

27. Private communication with Dr. J. D. Williams, Hughes Research Laboratories.

28. Beattie, J. R. and Matossian, J. N., "High Power Ion Thruster Technology," NAS-3-25553.

29. Rapp, D. and Englander-Golden, P., "Total Cross Sections for Ionization and Attachment in Gases by Electron Impact. I. Positive Ionization," *J. Chemical Physics*, Vol. 43, No. 5, p. 1464-1479.

30. Hayashi, M. ,"Determination of the electron-xenon total excitation cross-section, from threshold to 100 eV, from experimental values of Townsend's α," *J. Phys. D:Appl. Phys.*, 16 (1983) p.581-589.

31. Sai Baba, M., Lakshmi Narasimhan, T. S., Balasubramanian, R., and Mathews C. K., "Appearance potential and electron impact ionisation cross-sections of C_{60}," *International Journal of Mass Spectrometry and Ion Processes*, 114 (1992) p. R1-R8.

32. Private communication with Dr. C. K. Mathews, Indira Gandhi Centre for Atomic Research.

33. Gryzinski, M., "Two-Particle Collisions. I. General Relations for Collisions in the Laboratory System," *Physical Review*, Vol. 138, No. 2A, p. A305-A321.

34. Gryzinski, M., "Classical Theory of Atomic Collisions I. Theory of Inelastic Collisions," *Physical Review,* Vol. 138, No. 2A, p. A336-358.

35. Gryzinski, M., "Two-Particle Collisions II. Coulomb Collisions in the Laboratory System of Coordinadates," *Physical Review*, Vol. 138, No. 2A, p. A322-335.

36. Gryzinski, p. A343.

37. Wastberg, Bo and Rosen, Arne, "Electronic Structure of C_{60} and the Alkali Atom Containing Compounds of MC_{60}, M= Li, Na, K, Rb, Cs, and K_2C_{60}," *Physica Scripta*, 44, p.275-288.

38. Manousakis, Efstratios, "Electronic structure of C_{60} within the tight-binding approximation," *Physical Review B*, Vol. 44, No. 19, November 1991.

39. Samuel, Stuart, "On the Electronic Structure of C_{60}," CCNY-HEP-92/5, PREPRINT.

40. Abrefah, J., Olander, D. R., Balooch, M., and Siekhaus, W. J., "Vapor pressure of Buckminsterfullerene;" *Appl. Phys. Lett.*, 60 (11), March 1992.

41. Beattie, J. R., "Aerospace '91: Electric Propulsion," *Aerospace America*, December 1991.

42. Brophy, J. R., "Stationary Plasma Thruster Evaluation in Russia, " JPL Memorandum, March 15, 1992.